

Disentangling representations of retinal images with generative models

Sarah Müller^{1,2}, Lisa M. Koch^{1,2}, Hendrik P. A. Lensch³, and Philipp Berens^{1,2}

¹*Hertie Institute for AI in Brain Health, University of Tübingen, Germany*

²*Tübingen AI Center, Tübingen, Germany*

³*Département of Computer Science, University of Tübingen, Germany*
sar.mueller@uni-tuebingen.de

March 1, 2024

Abstract

Retinal fundus images play a crucial role in the early detection of eye diseases and, using deep learning approaches, recent studies have even demonstrated their potential for detecting cardiovascular risk factors and neurological disorders. However, the impact of technical factors on these images can pose challenges for reliable AI applications in ophthalmology. For example, large fundus cohorts are often confounded by factors like camera type, image quality or illumination level, bearing the risk of learning shortcuts rather than the causal relationships behind the image generation process. Here, we introduce a novel population model for retinal fundus images that effectively disentangles patient attributes from camera effects, thus enabling controllable and highly realistic image generation. To achieve this, we propose a novel disentanglement loss based on distance correlation. Through qualitative and quantitative analyses, we demonstrate the effectiveness of this novel loss function in disentangling the learned subspaces. Our results show that our model provides a new perspective on the complex relationship between patient attributes and technical confounders in retinal fundus image generation.

Keywords: disentanglement, generative model, representation learning, spurious correlation, causality, latent subspaces, retinal fundus images

1 Introduction

Retinal fundus images are medical images that capture the back of the eye and show the retina, optic disc, macula, and blood vessels. Due to their nature as color photographs acquired through the pupil, they are inexpensive, non-invasive, and quick to obtain, making them available even in resource-constrained regions. Despite their high availability, fundus images can be used to detect the presence not only of diseases of the eye, but also cardiovascular risk factors or neurological disorders using deep learning (Poplin et al., 2018; Kim et al., 2020; Rim et al., 2020; Son et al., 2020; Sabanayagam et al., 2020; Xiao et al., 2021; Rim et al., 2021; Nusinovici et al., 2022; Cheung et al., 2022; Tseng et al., 2023).

However, deep learning models require large datasets, and large medical imaging cohorts are often heterogeneous, with technical confounding being ubiquitous: for fundus images, variations in camera types, pupil dilation, image quality, and illumination levels can affect image generation, and biases due to hospital sites and patient study selection can lead to spurious feature correlations of these factors with biological variations in the data. Because deep learning models run the risk of learning shortcuts based on such spurious correlations (Geirhos et al., 2020) instead of specific patient-related image features (Fig. 1a), they may only perform well within the same distribution as the training data. For example, a retinal imaging dataset could be collected from two hospitals using cameras from different manufacturers (Fay et al., 2023). Camera A produces images appearing different in hue from camera B. The first hospital may treat predominantly Latin American patients, while the second hospital may treat predominantly Caucasians. In this scenario, it is simpler for a deep learning model to infer a patient’s ethnicity from a fundus image by recognizing hue rather than understanding the hidden causal relationship between ethnicity and phenotypic image features (Castro et al., 2020).

One solution for dealing with confounders in data is subspace learning, which combines representation learning and disentanglement. The subspaces can be constructed from a causal graph using domain knowledge about what influences the image generation process (Castro et al., 2020). In our case, we assume a simplified causal model that splits the fundus image generation into patient characteristics and technical factors (Fig. 1a). We

assume a shortcut connection due to spurious correlations between a patient attribute, such as ethnicity, and the camera as a technical factor (Fig. 1a, blue dashed arrow). To prevent shortcut learning, we aim to disentangle these factors of variation by encoding them into statistically independent latent subspaces that preferably match the ground truth generative factors (Bengio et al., 2013; Higgins et al., 2018).

One common strategy for acquiring disentangled representations makes use of generative image models such as VAEs (Kingma and Welling, 2014). Generative models offer a valuable inductive bias for representation learning by reconstructing images from the latent space and can be extended to learn independent subspaces (Fig. 1b) in an unsupervised or supervised manner (Higgins et al., 2017; Klys et al., 2018; Tschannen et al., 2018). Previous methods primarily focused on achieving a disentangled latent space, often neglecting the simultaneous pursuit of high-quality image generation. However, when latent space disentanglement and image generation are addressed simultaneously, generative image models provide a built-in interpretation method through controllable feature changes in the image space (Fig. 1d).

In this work, we close the gap of missing generative disentangled representation learning in conjunction with high-quality image generation in the domain of fundus images. Our primary objectives encompass three joint tasks: (1) disentangling learned representations, (2) preventing shortcut learning, and (3) enabling controllable high-resolution image generation.

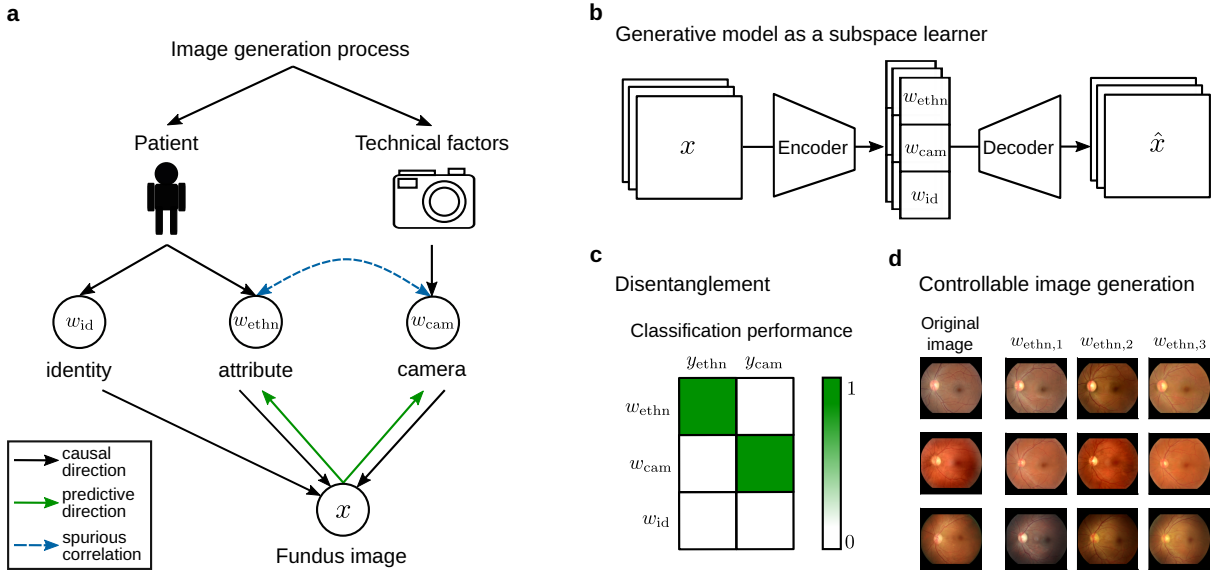


Figure 1: Disentangling representations of retinal images with generative models. In panel a, we present our conceptual causal graph outlining the image generation process (Fay et al., 2023). Within this framework, we break down retinal fundus image generation into patient-specific and technical factors of variation. We emphasize the potential shortcut for deep learning models when patient attributes exhibit spurious correlations with technical factors. In panel b, we introduce a strategy to circumvent shortcut learning by using a generative model as an independent subspace learner. Panel c shows our metric for disentanglement: an ideal confusion matrix between the available labels (columns) and the learned subspaces (rows). In panel d we demonstrate controllable fundus image generation by generating images from swapped ethnicity subspaces between the encoded original images in the first column.

2 Related work

Generative models for representation learning. Generative models such as VAEs are established methods for representation learning (Tschannen et al., 2018). However, it is difficult to use them for detailed high-resolution reconstructions, which are relevant in the field of retinal imaging, where fine details have a large impact on patient attribute or disease classification. Consequently, work on generative representation learning primarily focuses on learning low-dimensional latent spaces with specific properties rather than trying to generate accurate image reconstructions (Tschannen et al., 2018).

Generative adversarial networks (GANs), on the other hand, succeed in the generation of fine details in the image domain. Especially state-of-the-art GANs like StyleGAN2 (Karras et al., 2020) are able to create high-fidelity and high-resolution images. When labels are available, conditional GANs (Mirza and Osindero, 2014) and their variants (Odena et al., 2017; Miyato and Koyama, 2018) are the most established extensions for class-conditional image generation. However, conditional GANs mainly focus on generating realistic images and do not focus on

the independence of the latent space from the conditioned label.

InfoGAN (Chen et al., 2016) modifies the GAN objective to learn unsupervised disentangled representations by maximizing a lower bound of the mutual information (MI) between a subset of the latent variables and the observation. However, this extension does not guarantee that for complex image data, their induced factored latent codes are not dominated by shortcut features such as camera type. Furthermore, due to the unsupervised setting, disentangled features are analyzed post-hoc with human feedback, leading to potential non-identifiability (Locatello et al., 2019). Semi-StyleGAN (Nie et al., 2020), a special case of semi-supervised conditional GANs, extends the StyleGAN architecture to an InfoStyleGAN with an MI loss and addresses non-identifiability by adding a weakly supervised reconstruction term for partially available factors of variation.

Dependence estimators for disentanglement. In the field of disentanglement, a common goal is to use generative models as independent subspace learners, necessitating the estimation and minimization of statistical dependence between subspaces. Mutual Information (MI) is a viable measure for quantifying the mutual dependence between two variables, effectively capturing nonlinear dependencies. However, estimating MI in high-dimensional spaces remains a challenge. Earlier MI estimation approaches include non-parametric binning (Darbellay and Vajda, 1999), kernel density estimation (Härdle et al., 2006), likelihood-ratio estimation (Suzuki et al., 2008) and K-nearest neighbor estimation (Kraskov et al., 2004). These estimators typically do not scale well with sample size or dimension (Belghazi et al., 2018). Also, the gradient of these methods is difficult to calculate, which makes them inapplicable to back-propagation frameworks for MI optimization.

Therefore, recent work has focused on estimating bounds to establish tractable and scalable MI objectives. Most of the proposed approaches are lower bounds (Poole et al., 2019; Belghazi et al., 2018), which are not applicable to MI minimization problems. There is limited work on estimating MI upper bounds, and most of them are restrictive in the sense that they require the conditional distribution to be known (Alemi et al., 2017; Poole et al., 2019; Cheng et al., 2020).

Distance measures between distributions, such as the MI, provide a theoretically sound measure, but often require density estimation. To address this, non-parametric kernel method such as maximum mean discrepancy (MMD) (Sejdinovic et al., 2013) offer a principled alternative. MMD simplifies distance computation by using mean kernel embeddings of features, and is therefore also used to learn invariant representations, as in the Variational Fair Autoencoder (VFAE) (Louizos et al., 2017). Another non-parametric alternative to MI estimation is the use of adversarial classifiers, which solve the invariant subspace problem by solving the trade-off between task performance and invariance through iterative minimax optimization (Ganin and Lempitsky, 2015; Ganin et al., 2016; Xie et al., 2017). However, adversarial training adds an unnecessary layer of complexity to the learning problem Moyer et al. (2018) that does not scale well with multiple subspaces.

Disentanglement in medical image analysis. In medical imaging, disentangled representations are relevant to many research questions related to image synthesis, segmentation, registration, and causal- or federated learning, e.g., for disease decomposition, harmonization, or controllable synthesis. For a more comprehensive overview of the applications in medical imaging, we refer to Liu et al. (2022). For example, Fay et al. (2023) present a predictive approach to avoid shortcut learning for MRI data from different scanners. To minimize the dependencies between a task-specific factor (e.g. patient attribute) and a confounding correlated factor (e.g. scanner), they estimate a lower bound for MI. However, as mentioned earlier, a lower bound MI estimate is inconsistent to MI minimization tasks. In ICAM (Bass et al., 2020, 2021), the authors build on a VAE-GAN approach for image-to-image translation (Lee et al., 2018) to disentangle disease-relevant from disease-irrelevant features. However, disentanglement in ICAM requires longitudinal data, where patient images are available at different disease stages. In a similar approach, Ouyang et al. (2021) embed MRI images into independent anatomical and modality subspaces by image-to-image translation. Like ICAM, they have the data constraint that their method only works with images of the same patient from different modalities. In another attempt to explain classifier features, StyleX (Lang et al., 2021) integrates a classifier into StyleGAN training. They have a classifier-specific intermediate latent space and can visualize image features that are important for the classifier decision. Although the authors apply their approach to the retinal fundus domain, they do not address spurious correlation and shortcut learning.

3 Methods

This section introduces the proposed extensions to the generative model architecture and training constraints to disentangle the representations, prevent shortcut learning, and still enable controllable high-resolution image generation. First, we introduce the dataset, an encoder model and our disentanglement loss as preliminary steps towards the complete image generation pipeline.

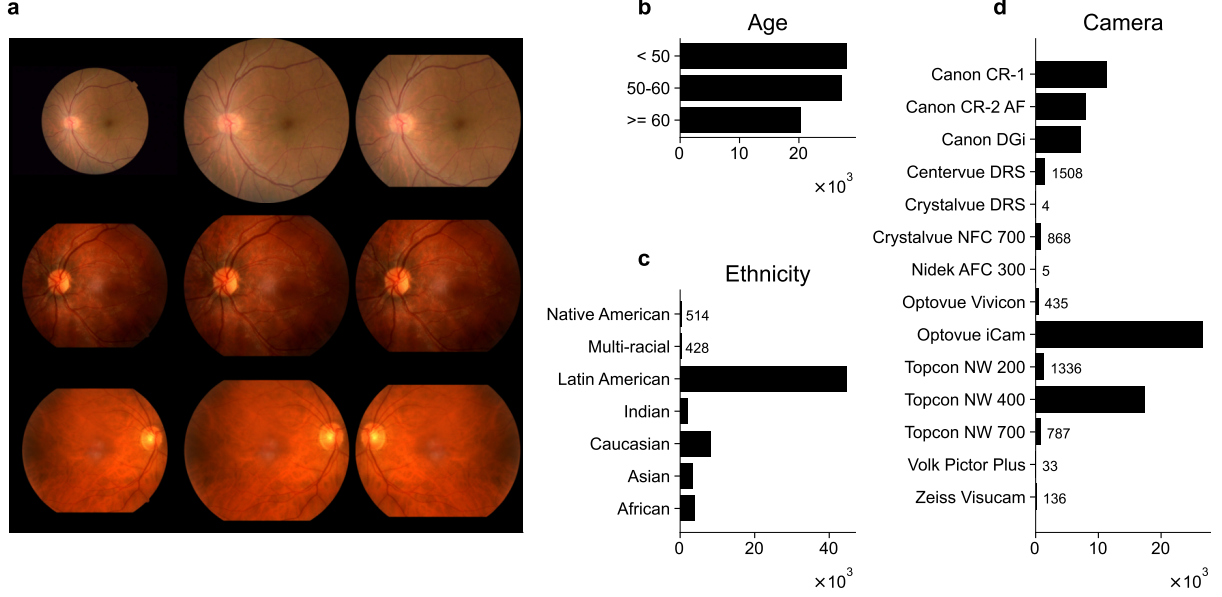


Figure 2: Image preprocessing and data distribution. In panel **a**, we outline our two-step preprocessing of fundus images. The first column displays original samples from the training set, while the second column exhibits images tightly cropped around the fundus circle. In the third column, we further cropped and flipped the images for consistency. The corresponding label distributions are visualized as histogram plots in panels **b-d**. Specifically, panel **b** illustrates the age group distribution across three classes, panel **c** showcases the ethnicity distribution, and panel **d** presents the camera distribution. For underrepresented categories, the number of images is shown next to the respective bars.

3.1 Data

We trained our models on retinal fundus images provided by EyePACS Inc. (Cuadros and Bresnick, 2009; Eye, 2008), an adaptable telemedicine system for diabetic retinopathy screening from California. All data was anonymized by the data provider. We filtered for healthy fundus images with no reported eye disease which were labelled as “good” or “excellent” quality. This resulted in 75,989 macula-centered retinal fundus images of 24,336 individual patients. For training, we split the data by patient-identity into 60% training, 20% validation, and 20% test sets.

The retinal fundus images in EyePACS are not standardized in aspect ratio and field of view (Fig. 2 **a**, first column). To do so, we cropped them to a tightly centered circle (Müller et al., 2023) (Fig. 2 **a**, middle column) and resized them to a resolution of 256×256 pixels. Furthermore, to address evident and unwanted factors of variation, we standardized the images by masking them to a uniform visible area, as many images had missing regions at the top and bottom. Additionally, we horizontally flipped the images to ensure that all optic discs were positioned on the left side (Fig. 2 **a**, last column).

Retinal fundus images from EyePACS come with extensive technical and patient-specific metadata. Here, we relied on age, ethnicity, and camera labels (Fig. 2 **b-d**). The camera labels in EyePACS include some duplicate manufacturer names, which we merged into the 14 classes (Fig. 2 **d**).

3.2 Encoder model for mapping factors of variation

We first considered the image encoding task by learning an encoder f_θ that maps images to a latent representation $f_\theta : \mathcal{X} \rightarrow \mathcal{W}$. We observed noisy image data $x \in \mathcal{X}$ obtained from an unknown image generation process $x = g(s)$, where $s = (s_1, s_2, \dots, s_k)$ are the underlying factors of variation. Our goal was to find a mapping $f_\theta : \mathbb{R}^m \rightarrow \mathbb{R}^d$ for a latent space $f_\theta(x) = w = (w_1, w_2, \dots, w_k)$ such that each factor of variation s_i can be recovered from the corresponding latent subspace $w_i \in \mathbb{R}^{d_i}$, $d = \sum_{i=1}^k d_i$, by a linear mapping $\hat{s}_i = C_{\psi_i} w_i$, but not from the other latent subspaces w_j for $j \neq i$.

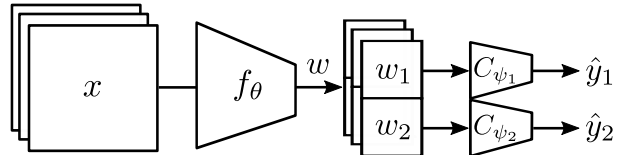


Figure 3: Encoder architecture. Feature encoder f_θ encodes input images x to feature vectors w . Each feature vector is split into two subspaces w_1 and w_2 by classification heads C_{ψ_1} and C_{ψ_2} .

Since we did not know the true underlying factors of variation, we used pseudo-labels from a labeled image dataset $\mathcal{D} = \{(x^{(i)}, y^{(i)})\}_{i=1}^N$, where $y^{(i)}$ is a vector of attribute labels. We assumed that these labels represent, in part, the true underlying factors of variation. We consider discrete attributes $y_k^{(i)} \in \mathbb{N}$, where $y_k^{(i)}$ is the label for the k^{th} attribute of the i^{th} sample.

In practice, we worked with retinal fundus images as our input domain \mathcal{X} , using a vector of available metadata as labels y . The goal was to encode the images into disentangled subspaces: $w = (w_1, w_2)$ for potentially highly correlated labels. To enforce attribute encoding in the subspaces, we defined a predictive model (Fig. 3) consisting of two parts: the feature encoder and the classification heads. The feature encoder f_θ maps input images $x \in \mathbb{R}^m$ to feature vectors $w \in \mathbb{R}^d$. Each feature vector was split into different subspaces w_1, \dots, w_K by a linear classification head C_{ψ_k} attached to each subspace k . Thus, optimizing the encoder to map to attribute subspaces was equivalent to optimizing the cross-entropy loss for each subspace individually:

$$(\theta^*, \psi^*) = \arg \min_{\theta, \psi} L_{\text{CE}}(\theta, \psi) \quad (1)$$

$$L_{\text{CE}}(\theta, \psi) = \frac{1}{K} \sum_{k=1}^K -y_k^T \log C_{\psi_k}(w_k). \quad (2)$$

3.3 Disentanglement loss

If the predictive model (Fig. 3) was only composed of an encoder and subspace classifiers, subspaces could correlate and share information. Therefore, we additionally penalized the presence of shared information with a disentanglement loss by minimizing the distance correlation (dCor) between subspaces.

Distance correlation (Székely et al., 2007) measures the dependence between random vectors. It is analogous to Pearson’s correlation but can also measure nonlinear dependencies between random vectors of arbitrary dimension. Moreover, the distance correlation is zero only if the random vectors are independent. We provide a toy example with linear and nonlinear dependencies in Appendix 6.1, where we compared the performance of minimizing distance correlation with minimizing linear dependence measures. In contrast to mutual information, distance correlation is easy to compute and does not require bound estimators. Furthermore, compared to adversarial classifiers, distance correlation showed better scalability when considering multiple subspaces, as adversarial classifiers add a learning problem for each subspace. For a more detailed background on dependence estimators we refer to the related work Sec. 2.

In practice, we computed the sample distance correlation measure (Székely et al., 2007) to disentangle subspaces with batch samples:

$$\text{dCor}(w_1, w_2) = \sqrt{\frac{\text{dCov}^2(w_1, w_2)}{(\text{dVar}^2(w_1) \text{dVar}^2(w_2))^{1/2}}} \quad (3)$$

We assumed n -dimensional batches of subspace vectors $w_1 \in \mathbb{R}^{n \times d_1}$ and $w_2 \in \mathbb{R}^{n \times d_2}$. We first mapped the subspace vectors into an $n \times n$ dimensional Euclidean space containing all pairwise distances from a batch:

$$A \in \mathbb{R}^{n \times n}, a_{j,k} = \|w_1^{(j)} - w_1^{(k)}\|_2, j, k = 1, 2, \dots, n \quad (4)$$

$$B \in \mathbb{R}^{n \times n}, b_{j,k} = \|w_2^{(j)} - w_2^{(k)}\|_2, j, k = 1, 2, \dots, n \quad (5)$$

$$(6)$$

The distance matrices for each subspace were then individually normalized by subtracting the row mean, column mean, and grand mean:

$$A_{j,k} := a_{j,k} - \bar{a}_{j,\bullet} - \bar{a}_{\bullet,k} - \bar{a}_{\bullet,\bullet} \quad (7)$$

$$B_{j,k} := b_{j,k} - \bar{b}_{j,\bullet} - \bar{b}_{\bullet,k} - \bar{b}_{\bullet,\bullet} \quad (8)$$

Based on the normalized subspace distance matrices, the sample squared distance covariance was simply the arithmetic average of the element-wise matrix product

$$\text{dCov}^2(w_1, w_2) = \frac{1}{n^2} \sum_{j=1}^n \sum_{k=1}^n A_{j,k} B_{j,k} \quad (9)$$

and the sample squared distance variance was the arithmetic average of the squared matrix elements

$$\text{dVar}^2(w_1) = \frac{1}{n^2} \sum_{j,k} A_{j,k}^2 \quad (10)$$

$$\text{dVar}^2(w_2) = \frac{1}{n^2} \sum_{j,k} B_{j,k}^2 \quad (11)$$

The distance correlation of two random variables was finally obtained by dividing the distance covariance by the product of the distance standard deviations (Eq. 3).

Hence, we extended the optimization problem to learn disentangled subspaces with an encoder architecture as follows:

$$(\theta^*, \psi^*) = \arg \min_{\theta, \psi} L_{CE}(\theta, \psi) + \lambda_{DC} L_{DC}(\theta) \quad (12)$$

$$L_{DC}(\theta) = \frac{1}{K} \sum_{i \neq k}^K \text{dCor}(w_k, w_i) \quad (13)$$

3.4 Measuring disentanglement

Measuring disentanglement in a latent space is a non-trivial task. While there is no universally accepted definition of disentanglement, but most agree on two main points (Carbonneau et al., 2022). Firstly, there is a consensus that representation factors should exhibit independence, a quality commonly denoted as **modularity**. This implies that a factor affects only a subset of the representation space, and only this factor affects this subspace. Moreover, the affected representation space by a factor should be as small as possible, a principle known as **compactness**. The last agreed-upon criterion is the information content or **explicitness**. In essence, a disentangled representation should completely describe all factors of interest. To assess disentanglement, three distinct families of metrics have been proposed: intervention-based, predictor-based, and information-based metrics (Carbonneau et al., 2022).

In our case, we opted for a predictor-based metric to evaluate both modularity and explicitness, excluding compactness from consideration because we fixed subspace dimensions. For our predictor, we employed a k-nearest neighbors (kNN) classifier with k=30. Using this classifier, we generated a confusion matrix, comparing subspaces with associated labels, for example ethnicity and camera (Fig. 4). Given the presence of unbalanced classes, we reported the accuracy improvement over chance level accuracy. With the confusion matrix, modularity is evident through high classification accuracy improvement for one factor (e.g. ethnicity) in only one subspace. Explicitness, on the other hand, becomes apparent when the accuracy improvement is notably high across the entire matrix. Consequently, when both modularity and explicitness are effectively addressed, the confusion matrix has high values along the main diagonal as well as low values on the off-diagonals (Fig. 4).

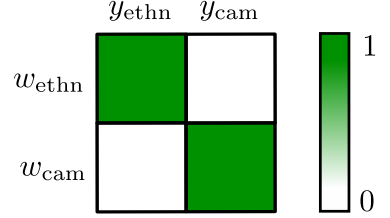


Figure 4: Example of a confusion matrix to measure disentanglement in terms of modularity and explicitness.

3.5 Generative image model

For the generative model, the overall goal was to generate realistic fundus images with potentially correlated labels from a disentangled latent space. We considered the image generation task by learning the mapping between two domains $M : \mathcal{X} \rightarrow \hat{\mathcal{X}}$ with a latent space model. We split M into two components, $M = d \circ g$, where the encoder/discriminator d maps to an intermediate latent representation $d : \mathcal{X} \rightarrow \mathcal{W}$ and the generator $g : \mathcal{W} \rightarrow \hat{\mathcal{X}}$ maps to the output image domain.

We chose to work with a StyleGAN2 architecture (Karras et al., 2020), a state-of-the-art generative adversarial network for high-fidelity and high-resolution images. The StyleGAN architecture has two features that makes it a potentially good candidate for disentanglement: (1) it consists of a mapping network $m : \mathcal{Z} \rightarrow \mathcal{W}$ that maps a latent vector into an intermediate space, which then controls the styles in each convolutional layer in the generator with adaptive instance normalization, and (2) it allows for the separation of fine-grained and coarse-grained features by a progressively growing generator.

We trained the generative image model with the standard minimax GAN loss together with StyleGAN’s path length regularization (Karras et al., 2020) on the generator and an R1 regularizer (Mescheder et al., 2018) as a gradient penalty on the discriminator for real data. The resulting optimization problem can then be expressed as:

$$L_{GAN}(\eta, \tau) = \mathbb{E}_{x \in \mathcal{X}} [\log(d_{\tau,0}(x))] + \mathbb{E}_{z \in \mathcal{Z}} [\log(1 - d_{\tau,0}(g_{\eta}(w)))] + \lambda_{PL} PL(\eta) - \lambda_{R1} R_1(\tau) \quad (14)$$

$$\eta^* = \arg \min_{\eta} L_{GAN}(\eta, \tau^*) \quad (15)$$

$$\tau^* = \arg \min_{\tau} -L_{GAN}(\eta^*, \tau) \quad (16)$$

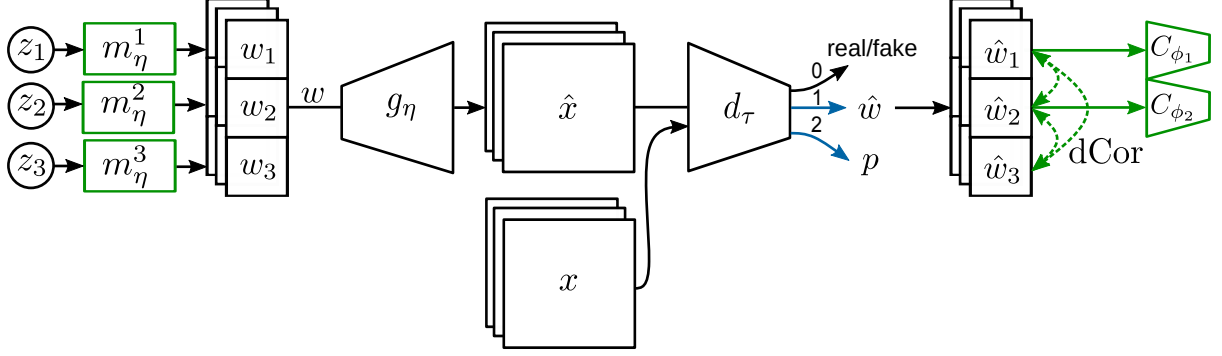


Figure 5: Generative image model with subspace constraints. For each image, we sample three individual latent codes from a standard normal distribution $z_k \sim \mathcal{N}(0, I_{d_k})$ and employ individual mapping networks $m_\eta^k : \mathcal{Z} \rightarrow \mathcal{W}_k$ to map them to intermediate latent spaces. The concatenation of all three subspaces $w = [w_1, w_2, w_3] \in \mathbb{R}^{d_1+d_2+d_3}$ serves as input to the generator $g_\eta : \mathcal{W} \rightarrow \mathcal{X}$. For **GAN-inversion**, we extend our discriminator with two additional heads: one for latent representation \hat{w} and another for a pixel feature vector p responsible for image encoding and pixel space reconstruction, respectively. For **subspace learning**, we introduce an individual mapping network for each subspace and incorporate label information for real images through classification heads for the first two subspaces. To prevent subspace correlation, we implement a penalty for the classification tasks using the average distance correlation (dCor) between the subspaces \hat{w}_k that the discriminator outputs.

Here, $d_{\tau,0}(x)$ is the discriminator’s estimate of the probability that the real data instance x is real, $g_\eta(w)$ denotes the generator’s output given w , and $d_{\tau,0}(g_\eta(w))$ is the discriminator’s estimate of the probability that a fake instance is real (Fig. 5).

As GANs were not originally designed for representation learning, they do not provide an encoder model. Therefore, we extended the StyleGAN2 architecture with an encoder to embed real images in the latest space for representation learning. Inspired by the work of invGAN (Ghosh et al., 2022), we extended the discriminator and also trained it as an encoder. We added two independent, fully connected layers and returned an estimate of the latent representation \hat{w} for our first inversion loss

$$L_w(\eta, \tau) = \mathbb{E}_{z \in \mathcal{Z}} [\|w - \hat{w}\|_2^2] = \mathbb{E}_{z \in \mathcal{Z}} [\|w - d_{\tau,1}(g_\eta(w))\|_2^2]. \quad (17)$$

We also incorporated the pixel space reconstruction loss from invGAN (Ghosh et al., 2022) to further impose consistency for the GAN-inversion and to ensure that the reconstruction of an image’s latent code is close to the original image in pixel space. As the definition of a meaningful distance function between real images and their reconstructions is a non-trivial task, they employ the discriminator also as a feature extractor (Ghosh et al., 2022). Therefore, we added a third head at the penultimate discriminator layer, which maps from an image to a pixel feature vector $f_p : \mathcal{X} \rightarrow p$ for our second GAN-inversion loss

$$L_p(\eta, \tau) = \mathbb{E}_{x \in \mathcal{X}} [\|f_p(x) - f_p(\hat{x})\|_2^2] = \mathbb{E}_{x \in \mathcal{X}} [\|d_{\tau,2}(x) - d_{\tau,2}(g_\eta(d_{\tau,1}(x)))\|_2^2]. \quad (18)$$

Because we have two forward passes through the decoder in Eq. 18, the pixel space reconstruction loss also serves as a cycle consistency loss.

For subspace learning, we modified the StyleGAN2 architecture to sample individual latent codes from a standard normal distribution $z_k \sim \mathcal{N}(0, I_{d_k})$ and learned individual 8-layer mapping networks for each subspace $m_\eta^k : \mathcal{Z}_k \rightarrow \mathcal{W}_k$ (Fig. 5, left), where each subspace can have a different dimensionality $w_k \in \mathbb{R}^{d_k}$. In setting up the generative image model, we assumed that we do not know all the underlying factors of variation or have access to their labels. Therefore, we provided the model with a free patient-identity subspace w_3 (Fig. 5), in which the encoder/discriminator can capture for further information required to reconstruct high-resolution retinal fundus images. As in the encoder model (Sec. 3.2), we encoded label information for real images by training linear classification heads C_{ψ_k} for the first two subspaces (Fig. 5, right). To avoid subspace correlation, we penalized the classification task with the mean of all distance correlation measures between subspaces \hat{w}_k that the discriminator outputs.

Hence, the overall objective was

$$\eta^* = \arg \min_{\eta} L_{\text{GAN}}(\eta, \tau^*) + \lambda_w L_w(\eta, \tau^*) + \lambda_p L_p(\eta, \tau^*) \quad (19)$$

$$(\tau^*, \psi^*) = \arg \min_{\tau, \psi} -L_{\text{GAN}}(\eta^*, \tau) + \lambda_w L_w(\eta^*, \tau) + \lambda_p L_p(\eta^*, \tau) + \lambda_C L_C(\tau, \psi) + \lambda_{\text{DC}} L_{\text{DC}}(\tau) \quad (20)$$

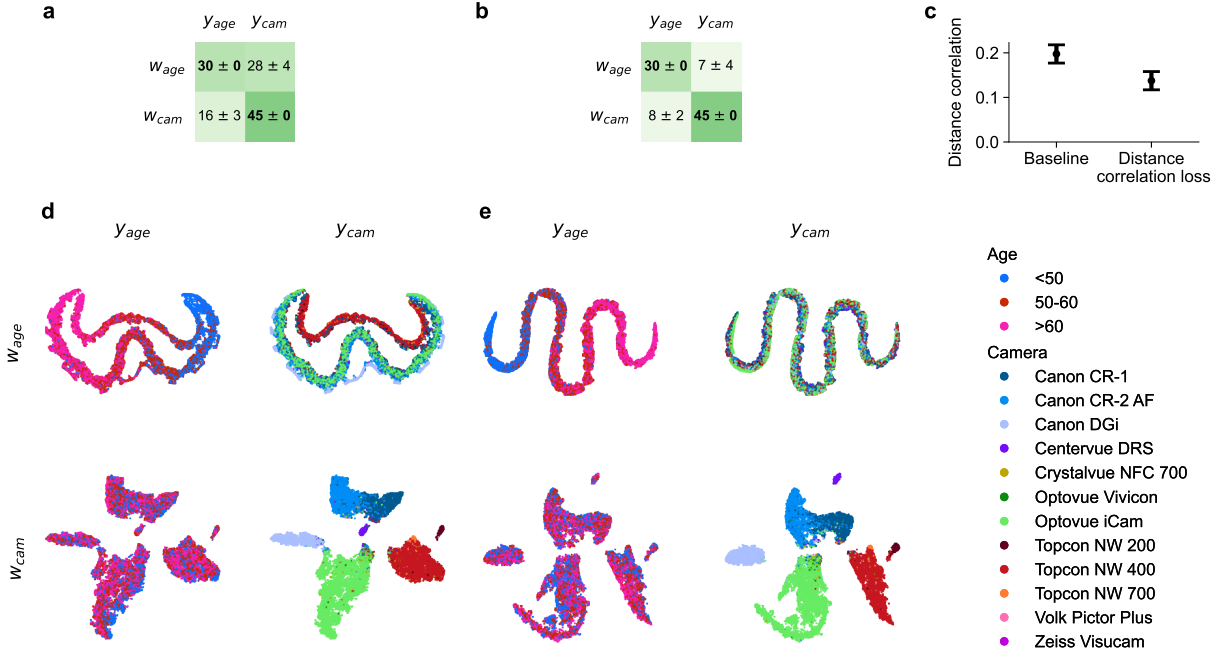


Figure 6: Disentanglement performance with encoder model for age-camera setup. We trained encoder models on retinal images, where the first subspace w_{age} encoded the age class y_{age} , and the second subspace w_{cam} encoded the camera class y_{cam} . In panels **a** and **b**, we present the improvement in kNN classifier accuracy over chance level accuracy. As a baseline model in **a**, we only trained linear classifiers on top of subspaces. In **b**, we further disentangle the subspaces using our distance correlation loss. Panel **c** illustrates the distance correlation measure between subspaces w_{age} and w_{cam} for both the baseline method and the method incorporating additional distance correlation minimization. In panels **d** and **e**, we provide t-SNE visualizations comparing a baseline model with a model incorporating disentanglement loss, respectively.

with the generator optimization in Eq. 19 and the discriminator optimization in Eq. 20. The discriminator, in its role as an encoder, also optimizes subspace losses on real images.

In practice, we optimized the objectives for the generator (Eq. 19) and the discriminator (Eq. 20) with batch estimates and stochastic gradient descent. Moreover, we used separate optimizers for generator and discriminator optimization. Appendix 6.4 contains additional information about the generative model training.

4 Results

We conducted empirical evaluations to assess the efficacy of our disentanglement loss in two distinct scenarios: (1) a predictive task and (2) a generative task, both performed on retinal fundus images. Our primary objective in both cases was to disentangle the technical factor camera from patient attributes age and ethnicity.

For each setting, we conducted two experiments, configuring the model to learn specific subspaces. In the initial experiment, the first subspace $w_{age} \in \mathbb{R}^4$ encoded age information, while the second subspace $w_{cam} \in \mathbb{R}^{12}$ captured camera-related details. In the second experiment, we designed the first subspace $w_{ethn} \in \mathbb{R}^8$ to encode ethnicity information, while the second subspace focused on camera-related features $w_{cam} \in \mathbb{R}^{12}$. The dimensionality of each subspace was selected based on the dimensions of the labels we aimed to encode.

We filtered for images where labels for these classes were available and ended up with 75,708 images (24,254 patients) for the first and 63,210 images (19,950 patients) for the second experiment (see Sec. 3.1 for details). For more information about predictive model training, see Appendix 6.3.

4.1 Learning disentangled subspaces with an encoder model

We first evaluated the effect of the distance correlation loss on the simplest representation learning setup for images: an encoder neural network that mapped retinal images to a latent subspace representation (Fig. 3). To encourage disentangled subspaces, we studied the effect of minimizing the distance correlation between them (Sec. 3.3). To this end, we compared 4 runs of two model configurations on the test data: a baseline model, in which we trained only linear classifiers for subspace encoding, and a model that additionally minimized the distance correlation between subspaces.

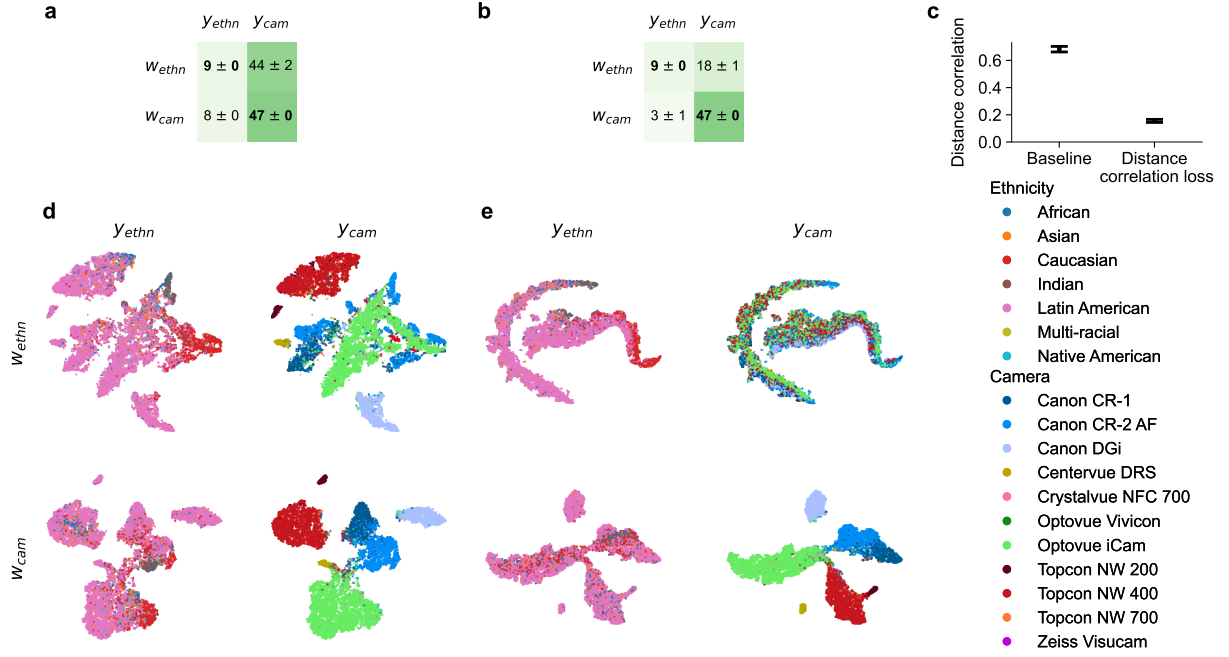


Figure 7: Disentanglement performance with encoder model for ethnicity-camera setup. We trained encoder models on retinal images, where the first subspace w_{ethn} encoded the ethnicity class y_{ethn} , and the second subspace w_{cam} encoded the camera class y_{cam} . In panels **a** and **b**, we present the improvement in kNN classifier accuracy over chance level accuracy. As a baseline model in **a**, we only trained linear classifiers on top of subspaces. In **b**, we further disentangle the subspaces using our distance correlation loss. Panel **c** illustrates the distance correlation measure between subspaces w_{age} and w_{cam} for both the baseline method and the method incorporating additional distance correlation minimization. In panels **d** and **e**, we provide t-SNE visualizations comparing a baseline model with a model incorporating disentanglement loss, respectively.

Our experiments suggest that the age and camera subspaces were heavily entangled in the baseline setting when disentanglement was not specifically enforced (Fig. 6 **a**), such that camera information was present in the age subspace and vice versa. Entanglement was visible by relatively high classification accuracy across subspaces (Fig. 6 **a**, off-diagonals). For example, camera type could be decoded from the age subspace w_{age} with a performance of 28% above chance level, compared to 45% in the dedicated camera subspace. When enforcing disentanglement by additionally minimizing the distance correlation between subspaces the cross-subspace classification performance (off-diagonals in Fig. 6 **b**) dropped, while the within-subspace classification was preserved (diagonals). In addition, the distance correlation between subspaces on the test data dropped as a direct consequence of our disentanglement loss. (Fig. 6 **c**) as a direct consequence of minimizing our disentanglement loss. We could also observe the disentanglement effect qualitatively in 2D t-SNE visualizations of the learned representations (Fig. 6 **d**, **e** for a baseline and disentangled model, respectively). In both the baseline and the disentangled model, the age subspace exhibited structure w.r.t. age, and the camera subspace encoded camera type well (diagonals in Fig. 6 **d**, **e**). In the baseline model, however, the age subspace also strongly encoded camera information (first row, second column in **d**).

In the second experiment, we observed an entanglement between the ethnicity and camera subspaces when employing the baseline method (Fig. 7 **a**). For the baseline method, comparable attribute performance was evident across subspaces (columns Fig. 7 **a**). For instance, camera decoding in the ethnicity subspace was at 44% accuracy improvement over chance level, compared to 47% for the dedicated camera subspace. Additionally, ethnicity decoding exhibited marginal improvement over chance level, with only 9% and 8%, respectively. This discrepancy could be attributed to the imbalance of our dataset, with 71% of patients being of Latin American descent (Fig. 2 **c**). Upon incorporating our disentanglement loss into the training process, distance correlation dropped notably (Fig. 7 **c**). Moreover, cross-subspace classification performance dropped (off-diagonals in Fig. 7 **a**), while within-subspace classification performance remained high (diagonals in Fig. 7 **a**). The impact of improved disentanglement was also evident in t-SNE visualizations. The baseline model exhibited camera clustering within the ethnicity subspace (Fig. 7 **d**), a phenomenon not observed in the model incorporating our disentanglement loss (Fig. 7 **e**).

4.2 Ablation study for disentanglement loss

We next conducted a sensitivity analysis for our prediction model with disentanglement loss and examined the effects of different hyperparameters. The subspace labels utilized for this analysis were age and camera. We specifically investigated the dimensionality of the subspace, the batch size, and the weight λ_{DC} assigned to the loss term targeting the minimization of distance correlation.

The initial hyperparameters were set as follows: a 4-dimensional age subspace w_{age} , a 12-dimensional camera subspace w_{cam} , a batch size of 512, and a loss weight of $\lambda_{DC} = 0.5$ for distance correlation. Subsequently, each hyperparameter was individually varied, and for each configuration, we trained four models with different random initializations. All evaluation metrics were then reported on the test set. This analysis provided insight into the robustness and performance of our disentanglement loss under varying hyperparameters.

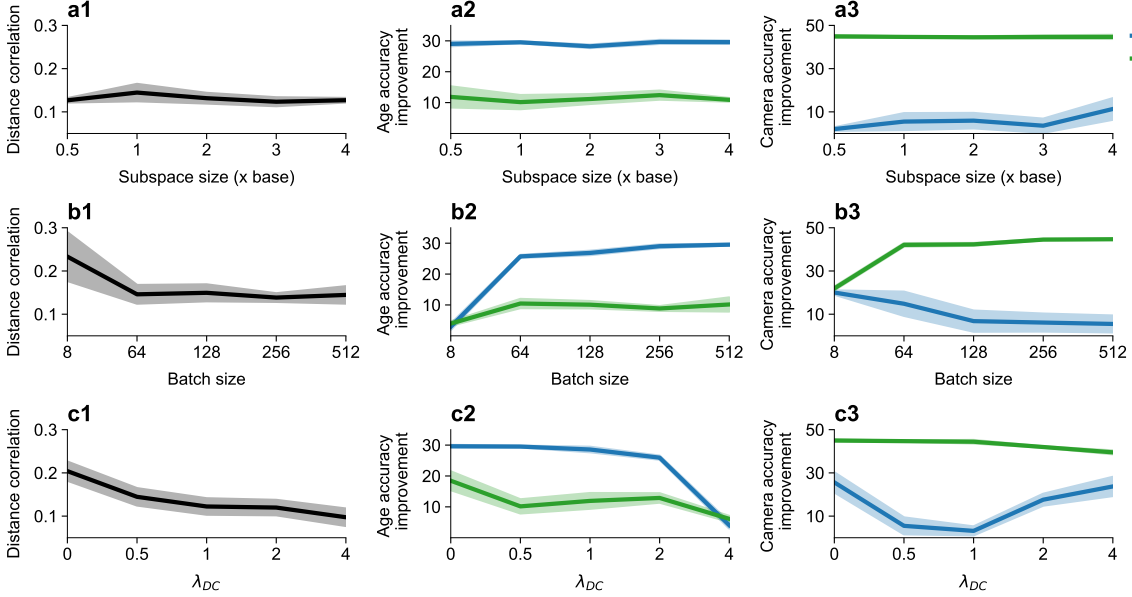


Figure 8: Impact of hyperparameters on disentanglement performance. In **a1-a3**, we present performance variations across different subspace sizes. Specifically, **a1** illustrates the distance correlation between subspaces, while **a2** and **a3** depict kNN accuracy improvement over chance level for age and camera, respectively. In **b1-b3**, we examine disentanglement performance under varying batch sizes. **c1-c3** focus on the impact of different distance correlation loss weights on disentanglement performance. All reported values are derived from test data and four models with different initializations.

The robustness of our disentanglement loss was evident across varied subspace sizes (Fig. 8 **a1-a3**). Interestingly, there were no discernible trends when we altered the subspace size by multiplying our initial sizes with different factors. Notably, one exception was observed in the accuracy improvement for the camera within the age subspace, particularly when employing a multiplier of 4 (Fig. 8 **a3**, blue curve). In this instance, the disentanglement problem becomes more challenging as we need to estimate the distance correlation between a 16- and a 48-dimensional subspace with a limited batch size of 512.

Smaller batch sizes impacted the disentanglement performance (Fig. 8 **b1-b3**). This effect was notable with the higher distance correlation values and worse decoding quality for a batch size of 8 compared to larger batch sizes (Fig. 8 **b1-b3**). Notably, for the age subspace, a batch size of 64 proved insufficient, as evident by the camera decoding not reaching a possible minimum observed with larger batch sizes (blue curve, Fig. 8 **b3**).

In the last ablation experiment, we explored the loss term λ_{DC} for distance correlation minimization (Fig. 8 **c1-c3**). The objective was to identify a valid range for this hyperparameter and to comprehend the consequences of deviating from this range. One non-surprising outcome was that the distance correlation became smaller with larger λ_{DC} (Fig. 8 **c1**). As expected, larger loss terms resulted in a collapse of subspace decoding. For example, the age accuracy improvement for both subspaces dropped below 10% (Fig. 8 **c2**). Also, the disentanglement performance for the camera deteriorated with larger λ_{DC} , as the accuracy improvement in both subspaces converged to 30-40% (Fig. 8 **c3**).

4.3 Learning disentangled subspaces with generative model

In the second part of the experiments, we extended our predictive model to a generative model, aiming to generate realistic retinal images from a disentangled latent space (Sec. 3.5).

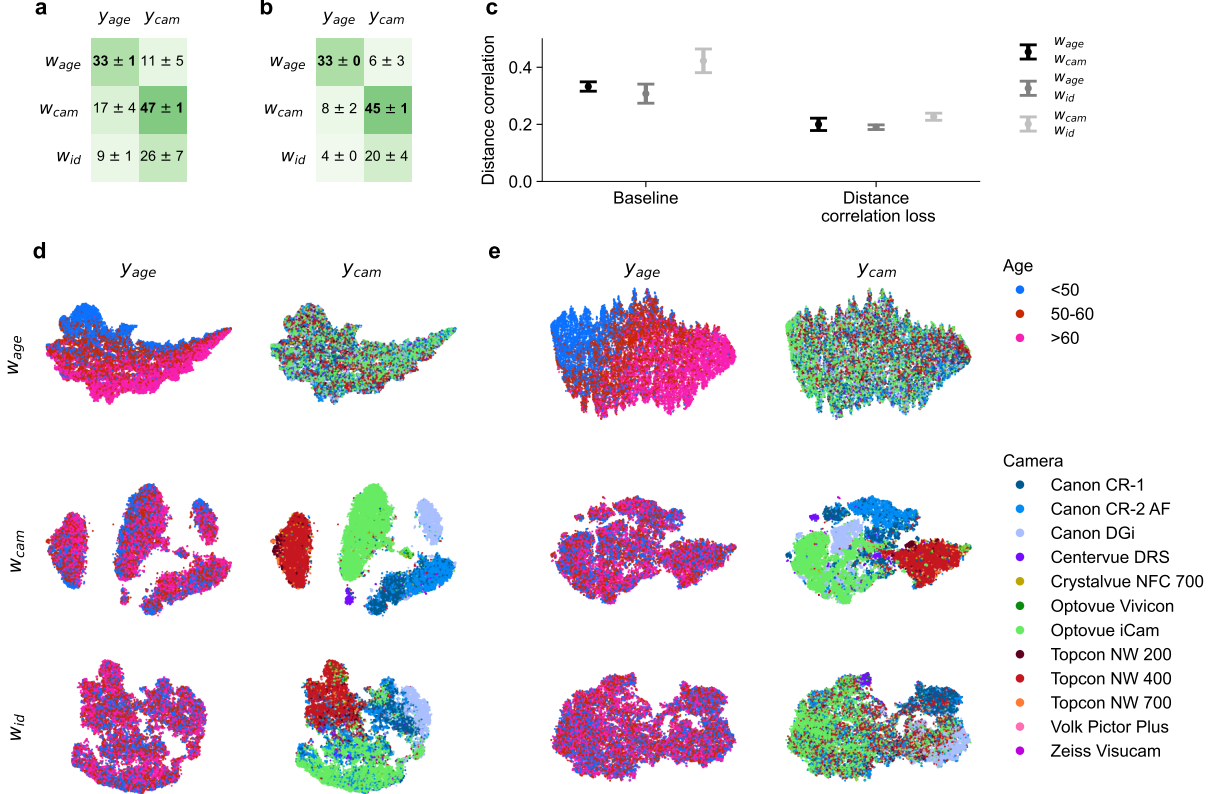


Figure 9: Disentanglement performance with generative model for age-camera setup. We trained generative models on retinal images, featuring three subspaces: w_{age} encoding the age class y_{age} , w_{cam} encoding the camera class y_{cam} , and w_{id} serving as a patient-identity subspace. In **a** and **b**, kNN classifier accuracy improvement over chance level accuracy is reported. The baseline model in **a** involved training linear classifiers solely on the first two subspaces. In **b**, we additionally disentangled the subspaces using our distance correlation loss. Panel **c** compares the distance correlation measure between subspaces and our two model configurations. Panels **d** and **e** present t-SNE visualizations of one baseline model and one trained generative model with the disentanglement loss, respectively.

As with the predictive model, as a baseline method, we learned subspaces by appending linear classifiers, addressing distinct classification tasks in each subspace. In the generative framework, we introduced an additional latent subspace dedicated to encoding the patient’s identity (Fig. 5), enhancing our ability to generate high-resolution and realistic retinal images. To ensure independence between these subspaces, we incorporated the minimization of distance correlation. Consequently, we aimed to minimize the distance correlation among three distinct subspace combinations. Notably, we specifically enforced independence for the patient-identity space, ensuring that it remained uncorrelated with the subspaces encoding age, ethnicity, or camera information.

We ran 5 models of each configuration – a baseline model and a model with distance correlation loss. However, during our experiments, we had to discard one model for evaluation as it did not converge properly, leaving us with 4 models for evaluation on the test data.

Our disentanglement loss also showed an effect when applied to a generative image model (Fig. 9). While the baseline model for the generative model already demonstrated relatively good disentanglement performance, the introduction of the distance correlation loss further enhanced the separation of subspaces. For example, for the baseline model, age information could be decoded from the camera subspace and vice versa (Fig. 9a, off-diagonals). Additionally, age, and particularly camera information, were still contained within the identity subspace of the baseline model (last row, Fig. 9a). Upon incorporating the distance correlation loss, cross-subspace classification performance (off-diagonals and last row, Fig. 9b) dropped, while within-subspace classification was preserved (diagonals). Consequently, the distance correlation between subspaces on the test data decreased (Fig. 9c), underscoring the effect of our disentanglement loss. The qualitative impact of disentanglement was further evident in t-SNE visualizations: for example, the camera labels clustered in the patient identity space for the baseline model, but the clustering became more mixed up when we incorporated the distance correlation loss (Fig. 9d,e).

In our second experiment, our objective was to disentangle ethnicity, camera, and patient-identity within three subspaces of a generative model (Fig. 10). Again the baseline model for the generative model already demon-

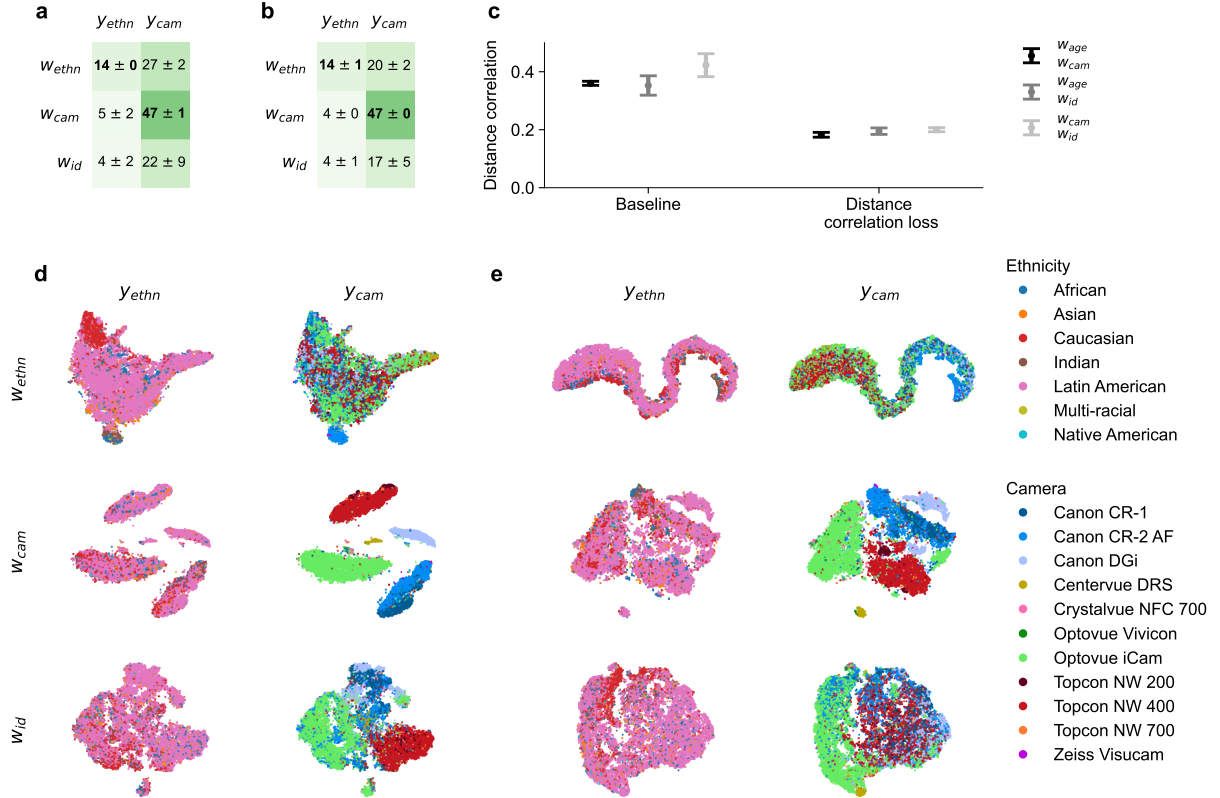


Figure 10: Disentanglement performance with generative model for ethnicity-camera setup. We trained generative models on retinal images, featuring three subspaces: w_{ethn} encoding the ethnicity class y_{ethn} , w_{cam} encoding the camera class y_{cam} , and w_{id} serving as a patient-identity subspace. In **a** and **b**, kNN classifier accuracy improvement over chance level accuracy is reported. The baseline model in **a** involved training linear classifiers solely on the first two subspaces. In **b**, we additionally disentangled the subspaces using our distance correlation loss. Panel **c** illustrates the distance correlation measure between subspaces, comparing the baseline method to the model additionally minimizing distance correlation. Panels **d** and **e** present t-SNE visualizations of one baseline model and one trained generative model with the disentanglement loss, respectively.

strated relatively good disentanglement performance compared to the encoder model (Fig. 7). However, the application of our disentanglement loss still demonstrated several effects. For instance, the accuracy improvement for camera decoding decreased by 7% for the ethnicity subspace and by 5% for the identity subspace on average (Fig. 10, **a** versus **b**). As a direct consequence of minimizing distance correlation between subspaces, this measure consistently decreased for all subspace combinations (Fig. 7 **c**). The t-SNE visualizations not only qualitatively showed the classification and disentanglement performance (Fig. 7 **d,e**), but also pointed us to a correlation in the ethnicity subspace between Indian patients (first row, first column) and the Canon CR-2 AF camera (first row, second column), as they both co-occur in the same clusters, even after incorporating our disentanglement loss. Another interesting finding was that the decoding performance of the ethnicity subspace for ethnicity exhibited a 5% improvement for the generative model compared to the encoder model (Fig. 7 **a,b**). This disparity may suggest that the generative model serves as a better feature extractor because of a better learning bias or a greater model capacity.

4.4 Realistic image generation and reconstruction

Next, we evaluated the image quality and the reconstruction performance of our generative model. As a baseline we chose a standard StyleGAN2 model with GAN-inversion losses, which we compared to models incorporating our additional losses for independent subspace learning. The baseline model was trained with a 32-dimensional latent space and a single mapping network. For the comparison models, we chose our \mathcal{W} -spaces to be either 32- or 36-dimensional for the age-camera-identity and ethnicity-camera-identity setups, respectively. All models generated retinal fundus images with a resolution of 256×256 .

We were able to generate realistic images and accurately reconstruct real images: generated retinal fundus images from randomly sampled latent vectors showed retinas of varying pigmentation with an optic disc and macula (Fig. 11 **a**). The fine vascular structures showed different patterns, resulting in a general appearance similar to the original data distribution. However, on closer inspection, the generated vasculature was not always intact.

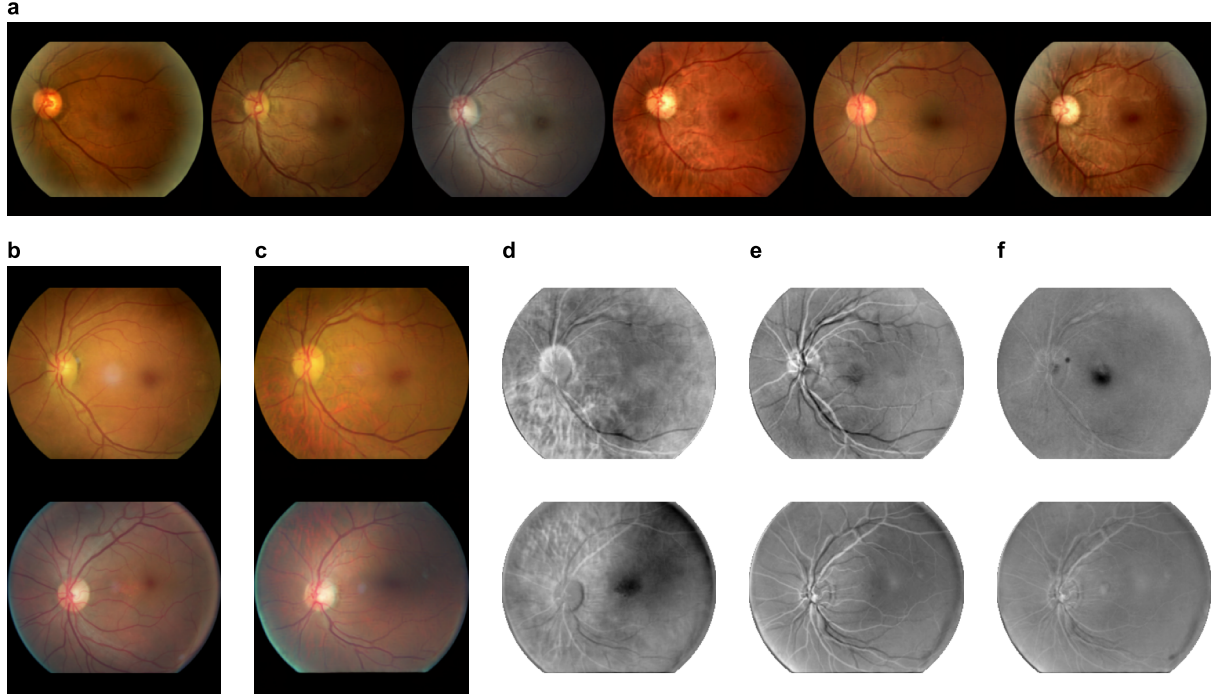


Figure 11: Qualitative image generation and inversion performance. We present a qualitative assessment of image generation performance for one model of configuration (C) (Tab. 1). In panel **a**, we show images generated from randomly sampled latent vectors. Panel **b** features retinal image samples from the test dataset. In panel **c**, we display the corresponding reconstructions produced by the generative model. Additionally, we show the difference maps for each of the RGB channels in **d-f**.

Furthermore, the inversion performance of the model was qualitatively robust, especially for coarse structures. A visual comparison of some retinal images (Fig. 11 **b**) with their reconstructions (Fig. 11 **c**) showed similarities in pigmentation, shape, position of the macula, and general vascular structure. However, detailed examination of the difference maps (Fig. 11 **d-f**) revealed some inaccuracies in the precise reconstruction of the vasculature, especially for thin vessels.

In a quantitative evaluation we confirmed that the image quality was not affected by additional constraints for learning disentangled subspaces (Tab. 1). To measure image quality, we used Frechet Inception Distance (FID) (Heusel et al., 2018; Parmar et al., 2022), which assesses differences between the distribution densities of real and fake images in the feature space of an InceptionV3 classifier (Simonyan and Zisserman, 2015). For the baseline model, we measured an FID score of 14 (Tab. 1, model A). Subsequent models incorporating subspace classifiers showed FID scores similar to the baseline, with no notable decrease for models also incorporating the distance correlation loss (Tab. 1, B versus C or D versus E).

Furthermore, we examined how additional subspace losses affected the image reconstruction performance, by reporting our inversion losses L_w and L_p for image encoding and pixel space reconstruction, respectively. As expected, image encoding L_w consistently showed a slight degradation for models that we jointly optimized with our disentanglement loss (Tab. 1, model C and E). In contrast, the pixel space reconstruction loss L_p remained comparable across all configurations. However, L_p showed worse mean performance with high variances for some model configurations (Tab. 1, model A and D), suggesting that this loss could potentially benefit from a higher weight, which was also visible in the qualitative pixel space reconstruction difference maps (Fig. 11 **d-f**).

Table 1: Image quality and inversion performance. For different model configurations we report the FID scores between the training dataset and the generated images, along with the inversion losses L_w and L_p . All metrics are reported on the test set as the average over four models with different weight initializations.

Model configuration	FID ↓	L_w ↓	L_p ↓
(A) Baseline GAN with inversion losses	14 ± 3	0.025 ± 0.01	0.010 ± 0.010
(B) Model A + subspace classifiers (age, camera)	13 ± 3	0.028 ± 0.01	0.002 ± 0.002
(C) Model B + distance correlation loss	11 ± 2	0.031 ± 0.01	0.006 ± 0.006
(D) Model C + subspace classifiers (ethnicity, camera)	12 ± 2	0.025 ± 0.01	0.010 ± 0.020
(E) Model D + distance correlation loss	13 ± 2	0.027 ± 0.01	0.002 ± 0.001

4.5 Controllable fundus image generation

In our final experiment, we explored how disentangled subspaces of a generative model influence the generation of retinal fundus images. We started by embedding the original images into latent spaces using our generative model. Because our models were trained with a disentanglement loss, we were able to partition partitioned these latent spaces into three independent subspaces: the first subspace represented a patient attribute (age or ethnicity), the second subspace encoded the camera, and the third subspace represented patient-identity information. Subsequently, we performed subspace swapping by exchanging the subspace embeddings of different retinal images, allowing us to observe the effect of each subspace on image generation.

The subspace swapping yielded matrices of image reconstructions from different latent subspace combinations (Fig. 12 and Fig. 13). In each column, one fundus image subspace was replaced with another one. Consequently, the main diagonals in the resulting matrices represent reconstructions of the original images, while the off-diagonals show reconstructions where one subspace was replaced by the subspace of another retinal image.

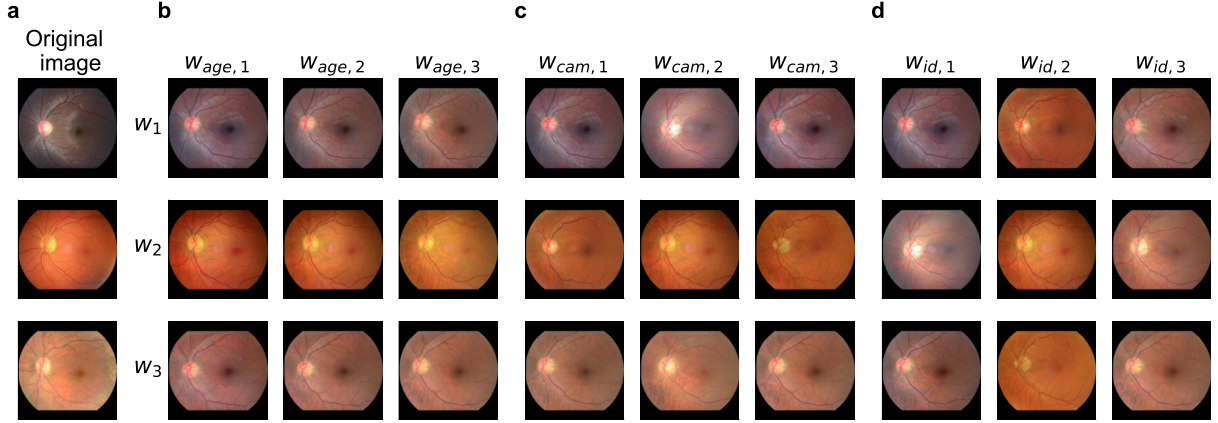


Figure 12: Reconstructions of swapped latent subspaces for age-camera-identity disentanglement. In panel a, original fundus images are presented alongside their respective reconstructions in panels b-d. Each column in panels b-d corresponds to the exchange of age, camera, or identity subspaces between the image encodings of panel a. The main diagonals in panels b-d show reconstructions of the images in a, while the off-diagonals illustrate reconstructions where one subspace has been replaced with the subspace indicated in the column header.

For the qualitative analysis, we selected the best of our age-camera-identity models based on disentanglement performance. The original images were randomly sampled from the test set, with the following age and camera labels (Fig. 12, a): (1) 22, Topcon NW 400, (2) 52, Optovue iCam, (3) 76, Canon CR-1. By swapping different subspaces, we generated matrices of image reconstructions from different latent subspace combinations (Fig. 12 b-d). Swapping the age subspace between image encodings for reconstruction led to subtle feature changes (Fig. 12 b). Notably, bright and reflective features around the thickest vasculature were observed, which tended to fade for age subspaces belonging to an older person (Fig. 12 b, first row). These bright and sheen structures are particularly common in the young population and tend to decrease with age (Williams, 1982). We also investigated the impact of changes in the camera subspace on fundus image generation (Fig. 12 c). In this model, each column representing a different camera subspace displayed subtle feature changes, occasionally affecting identity features such as the optic disc and vasculature (second column, Fig. 12 c). Finally, we swapped the identity subspaces, which were the largest subspaces with 16 dimensions each (Fig. 12 d). The idea was to store all remaining information relevant to the image reconstruction in this subspace. As intended, we observed a similar appearance of vasculature, optic disc, and fundus pigmentation in each patient-identity column (Fig. 12 d, columns).

We also provide quantitative evidence that the age subspace indeed influences image generation with relevant age features. To quantitatively assess the controllable image generation, we trained an image classifier on the task of predicting age from image reconstructions of our four GAN models. For detailed information about the training and testing procedures, please refer to Appendix 6.5. We tested the classifier models on a 3-class problem (< 50 , $50 - 60$, ≥ 60) and a simpler 2-class problem distinguishing young from old patients (≤ 40 , ≥ 65). These two classification problems are almost balanced, with chance level accuracies of 37% for the 3-class problem and 57% for the 2-class problem. For testing, we evaluated the classification model in three scenarios: standard evaluation on test data, evaluation on reconstructed images from swapped age subspaces and their corresponding new age labels, and as a reference, we reconstructed images from swapped age subspaces but evaluated the classification performance against the original age labels. The third evaluation method ensured that the age information was not contained in the other subspaces. Comparing the three scenarios for both classification problems, we demonstrated that the age subspace indeed influenced image generation with the relevant features, as age predictions changed correctly when we swapped age subspaces. For example, in the 3-class problem, the

Table 2: Quantitative age space performance. In an image classification setting, we demonstrate the influence of the age subspace on image generation by capturing relevant features. We trained image classifiers using reconstructions from our 4 GAN models on the 3-class age problem. Subsequently, we tested the classifiers on the 3-class problem (< 50 , $50 - 60$, ≥ 60) and a simpler 2-class problem (≤ 40 , ≥ 65). Here, we present the mean and standard deviation of classification performances, illustrating how age predictions correctly changed when we swapped age subspaces.

classification task	test configuration	accuracy in %
3-class problem	standard	70 ± 1
	swapped age subspaces and labels	66 ± 2
	swapped age subspaces, original labels	40 ± 0
2-class problem	standard	87 ± 4
	swapped age subspaces and labels	85 ± 6
	swapped age subspaces, original labels	47 ± 2

performance dropped only from 70% to 66% for swapped age subspaces, compared to 40% for the wrong age label assignments (Tab. 2). Similarly, in the 2-class problem, we observed a drop from only 87% to 85%, compared to an accuracy of 47% for the wrong labels (Tab. 2).

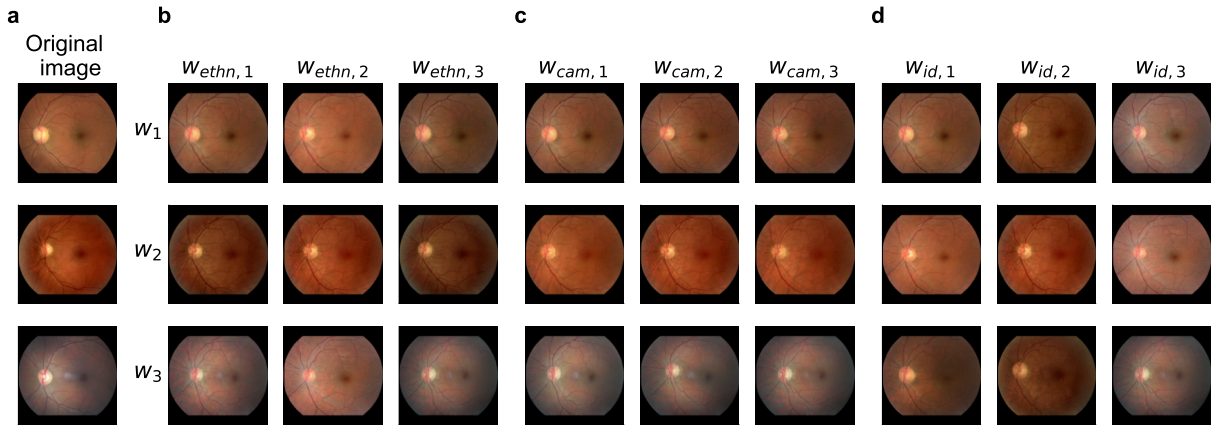


Figure 13: Reconstructions of swapped latent subspaces for ethnicity-camera-identity disentanglement. In panel **a**, original fundus images are presented alongside their respective reconstructions in panels **b-d**. Each column in panels **b-d** corresponds to the exchange of ethnicity, camera, or identity subspaces between the image encodings of panel **a**. The main diagonals in panels **b-d** show reconstructions of the images in **a**, while the off-diagonals illustrate reconstructions where one subspace has been replaced with the subspace indicated in the column header.

In a second experiment, we explored the performance of subspace swaps using our best ethnicity-camera-identity disentanglement model (Fig. 13). For this experiment, we randomly sampled three patients from the test set with the following ethnicity and camera labels (Fig. 13 **a**): (1) African, Topcon NW 400, (2) Caucasian, Optovue iCam, (3) Latin American, Canon CR-1. Swapping ethnicity subspaces had a qualitatively stronger visual effect on the image generation than swapping age subspaces (Fig. 13 **b**). In this case, the fundus pigmentation changed for different ethnicity subspaces, which is biologically plausible given the association between retinal pigmentation and ethnicity (Rajesh et al., 2023). However, some ethnicity subspace swaps also altered patient-identity features, such as the appearance of the vasculature (Fig. 13 **b**, last column). The camera subspace swaps exhibited only subtle visual feature changes, occasionally affecting identity features like the vasculature or the optic disc (Fig. 13 **c**, first column). When we changed the identity subspace, identity features (vasculature, optic disc) changed as intended (Fig. 13 **d**, rows).

5 Discussion

In this work, we focused on bridging the gap between existing generative models and disentangled representation learning for high-quality fundus image generation. We addressed the challenge of solving three joint tasks: (1) disentangling representations, (2) preventing shortcut learning, and (3) enabling controllable high-resolution image generation. To achieve this, we drew on recent advances in generative modeling and introduced a subspace GAN as a controllable population model for retinal fundus images. Our approach included the introduction of a novel disentanglement loss based on distance correlation. Through both qualitative and quantitative analyses,

we successfully demonstrated the effectiveness of our disentangled subspaces within a generative model. Our approach is not only applicable to the field of medical imaging. The general prerequisites for our method can also be fulfilled in other areas: prior knowledge of confounding factors in the image generation process and labels for the primary task and the confounding factor.

While our model shows excellent image generation performance with disentangled latent representations, some limitations should be acknowledged. One limitation is that the image reconstructions of our generative model showed deficits in capturing fine details, which is particularly evident in the accuracy of the vascular reconstructions. Interestingly, inherent correlations within the dataset pose a challenge for any disentanglement setup. Our experiments revealed that disentangling age from the camera was more straightforward than disentangling ethnicity from the camera, and that performance was limited by the strong correlation between ethnicity and camera in the EyePACS dataset (Träuble et al., 2021; Funke et al., 2022; Roth et al., 2023). In addition, it was challenging to disentangle the free identity space from the camera information. This difficulty may stem from the fact that these represent the largest subspace combinations, spanning 12- and 16-dimensional spaces, thus posing the greatest challenge for distance correlation estimation. Additionally, it is conceivable that camera features are correlated with other dataset features relevant to retinal fundus image generation, further complicating disentanglement.

Moreover, our distance correlation-based disentanglement loss introduced some challenges. First, our model architecture made it necessary to find a suitable balance between the disentanglement loss and the image generation task, and over-weighting the disentanglement loss could lead to poor image generation performance. Second, our disentanglement loss also introduced some technical challenges. Notably, distance correlation computation is sensitive to batch size, necessitating the introduction of a ring buffer for multi-GPU training (Appendix 6.4). However, the size of the ring buffer was constrained by the need to balance stored batches from the past and a model that is updated every step. Furthermore, driven by distance correlation estimation, we used small latent space sizes that still enable high-quality retinal image generation. Consequently, distance correlation poses a limitation on scaling up the latent space. Larger latent space sizes would require correspondingly larger batch sizes for accurate distance correlation estimation. This interdependence prompts a deeper exploration of the dynamics between the data ring buffer and latent space size to enhance our understanding of their collective impact on model performance.

In this study, our focus was exclusively on healthy fundus images due to the additional complexity that would have been introduced by reconstruction of disease features. However, the issue of spurious correlation between disease and technical features is a practical challenge that we aim to tackle in future work. Moreover, regardless of the fact that we deliberately chose to minimize the distance correlation as the disentanglement loss, alternative measures such as MMD and MI bounds or the use of adversarial classifiers can offer advantages, especially in terms of batch size or convergence time. We intend to investigate and compare these methods in the context of subspace disentanglement for medical images in future studies. In this work, we relied on labeled data to encode information into subspaces. Therefore, another compelling avenue for future research is to explore weakly supervised learning approaches, where we could apply a classification loss only on a subset of the training data, in addition to our disentanglement loss. This exploration could potentially yield effective results even on minimally labeled data.

In conclusion, our study presents an interpretable solution for modeling simple causal relationships for a medical dataset, aiming to mitigate shortcut learning arising from spurious correlations. We hope that this research provides a foundational approach for tackling confounded datasets and contributes to the ongoing exploration of methodologies towards comprehending the interplay between patient attributes and technical confounders.

Acknowledgements

We thank Holger Heidrich for discussing project directions and implementation details. We also thank Patrick Köhler, Kyra Kadhim, Simon Holdenried-Krafft, and Jeremiah Fadugba for helpful discussions and Kyra Kadhim, Julius Gervelmeyer, and Holger Heidrich for comments on the manuscript. This work was supported by the Deutsche Forschungsgemeinschaft under Germany’s Excellence Strategy – Excellence Cluster ”Machine Learning — New Perspectives for Science”, EXC2064/1 — Project number 390727645) and the Hertie Foundation. This research utilized compute resources at the Tübingen Machine Learning Cloud, INST 37/1057-1 FUGG. Philipp Berens is a member of the Else Kröner Medical Scientist Kolleg ”ClinbrAIn: Artificial Intelligence for Clinical Brain Research”. The authors thank the International Max Planck Research School for Intelligent Systems (IMPRS-IS) for supporting Sarah Müller.

References

- EyePACS digital retinal grading protocol (EyePACS), 2008. URL <https://www.eyepacs.org/consultant/Clinical/grading/EyePACS-DIGITAL-RETINAL-IMAGE-GRADING.pdf>.
- Alexander A. Alemi, Ian Fischer, Joshua V. Dillon, and Kevin Murphy. Deep Variational Information Bottleneck. In *International Conference on Learning Representations (ICLR)*, 2017.
- Cher Bass, Mariana da Silva, Carole Sudre, Petru-Daniel Tudosiu, Stephen M Smith, and Emma C Robinson. ICAM: Interpretable Classification via Disentangled Representations and Feature Attribution Mapping. In *Advances in Neural Information Processing Systems*, 2020.
- Cher Bass, Mariana da Silva, Carole Sudre, Logan ZJ Williams, Petru-Daniel Tudosiu, Fidel Alfaro-Almagro, Sean P Fitzgibbon, Matthew F Glasser, Stephen M Smith, and Emma C Robinson. ICAM-reg: Interpretable Classification and Regression with Feature Attribution for Mapping Neurological Phenotypes in Individual Scans. In *Medical Imaging with Deep Learning*, 2021.
- Mohamed Ishmael Belghazi, Aristide Baratin, Sai Rajeshwar, Sherjil Ozair, Yoshua Bengio, Aaron Courville, and Devon Hjelm. Mutual Information Neural Estimation. In *Proceedings of the 35th International Conference on Machine Learning*, 2018.
- Yoshua Bengio, Aaron Courville, and Pascal Vincent. Representation learning: A review and new perspectives. *IEEE Transactions on Pattern Analysis and Machine Intelligence*, 2013.
- Marc-André Carboneau, Julian Zaidi, Jonathan Boilard, and Ghyslain Gagnon. Measuring Disentanglement: A Review of Metrics. *IEEE Transactions on Neural Networks and Learning Systems*, 2022.
- Daniel C. Castro, Ian Walker, and Ben Glocker. Causality matters in medical imaging. *Nature Communications*, 2020.
- Xi Chen, Yan Duan, Rein Houthooft, John Schulman, Ilya Sutskever, and Pieter Abbeel. InfoGAN: Interpretable Representation Learning by Information Maximizing Generative Adversarial Nets. In *Advances in Neural Information Processing Systems*, 2016.
- Pengyu Cheng, Weituo Hao, Shuyang Dai, Jiachang Liu, Zhe Gan, and Lawrence Carin. CLUB: A Contrastive Log-ratio Upper Bound of Mutual Information. In *Proceedings of the 37th International Conference on Machine Learning*, 2020.
- Carol Y Cheung, An Ran Ran, Shujun Wang, Victor TT Chan, Kaiser Sham, Saima Hilal, Narayanaswamy Venketasubramanian, Ching-Yu Cheng, Charumathi Sabanayagam, Yih Chung Tham, et al. A deep learning model for detection of alzheimer’s disease based on retinal photographs: a retrospective, multicentre case-control study. *The Lancet Digital Health*, 2022.
- Jorge A Cuadros and George Bresnick. EyePACS: An Adaptable Telemedicine System for Diabetic Retinopathy Screening. *Journal of Diabetes Science and Technology*, 2009.
- G.A. Darbellay and I. Vajda. Estimation of the information by an adaptive partitioning of the observation space. *IEEE Transactions on Information Theory*, 1999.
- William Falcon and The PyTorch Lightning team. PyTorch Lightning, March 2019.
- Louisa Fay, Erick Cobos, Bin Yang, Sergios Gatidis, and Thomas Küstner. Avoiding Shortcut-Learning by Mutual Information Minimization in Deep Learning-Based Image Processing. *IEEE Access*, 2023.
- Christina M. Funke, Paul Vicol, Kuan-Chieh Wang, Matthias Kümmerer, Richard Zemel, and Matthias Bethge. Disentanglement and Generalization Under Correlation Shifts. In *ICLR 2022 workshop on Objects, Structure and Causality*, 2022.
- Yaroslav Ganin and Victor Lempitsky. Unsupervised Domain Adaptation by Backpropagation. In *Proceedings of the 32nd International Conference on Machine Learning*, 2015.
- Yaroslav Ganin, Evgeniya Ustinova, Hana Ajakan, Pascal Germain, Hugo Larochelle, François Laviolette, Mario Marchand, and Victor Lempitsky. Domain-Adversarial Training of Neural Networks. *Journal of Machine Learning Research*, 2016.
- Robert Geirhos, Jörn-Henrik Jacobsen, Claudio Michaelis, Richard Zemel, Wieland Brendel, Matthias Bethge, and Felix A. Wichmann. Shortcut learning in deep neural networks. *Nature Machine Intelligence*, 2020.
- Partha Ghosh, Dominik Zietlow, Michael J. Black, Larry S. Davis, and Xiaochen Hu. InvGAN: Invertible GANs. In *Pattern Recognition*, 2022.

- Wolfgang Karl Härdle, Marlene Müller, Stefan Sperlich, and Axel Werwatz. *Nonparametric and Semiparametric Models*. Springer Berlin, Heidelberg, 2006.
- Kaiming He, Xiangyu Zhang, Shaoqing Ren, and Jian Sun. Deep Residual Learning for Image Recognition. In *Conference on Computer Vision and Pattern Recognition*, 2016.
- Martin Heusel, Hubert Ramsauer, Thomas Unterthiner, Bernhard Nessler, and Sepp Hochreiter. GANs Trained by a Two Time-Scale Update Rule Converge to a Local Nash Equilibrium. In *Advances in Neural Information Processing Systems*, 2018.
- Irina Higgins, Loic Matthey, Arka Pal, Christopher Burgess, Xavier Glorot, Matthew Botvinick, Shakir Mohamed, and Alexander Lerchner. beta-VAE: Learning Basic Visual Concepts with a Constrained Variational Framework. In *International Conference on Learning Representations*, 2017.
- Irina Higgins, David Amos, David Pfau, Sebastien Racaniere, Loic Matthey, Danilo Rezende, and Alexander Lerchner. Towards a Definition of Disentangled Representations, 2018.
- Tero Karras, Samuli Laine, Miika Aittala, Janne Hellsten, Jaakko Lehtinen, and Timo Aila. Analyzing and Improving the Image Quality of StyleGAN. In *Conference on Computer Vision and Pattern Recognition*, 2020.
- Yong Dae Kim, Kyoung Jin Noh, Seong Jun Byun, Soochahn Lee, Tackeun Kim, Leonard Sunwoo, Kyong Joon Lee, Si-Hyuck Kang, Kyu Hyung Park, and Sang Jun Park. Effects of hypertension, diabetes, and smoking on age and sex prediction from retinal fundus images. *Scientific reports*, 2020.
- Diederik P Kingma and Max Welling. Auto-Encoding Variational Bayes. In *International Conference on Learning Representations*, 2014.
- Jack Klys, Jake Snell, and Richard Zemel. Learning Latent Subspaces in Variational Autoencoders. In *Advances in Neural Information Processing Systems*, 2018.
- Alexander Kraskov, Harald Stögbauer, and Peter Grassberger. Estimating mutual information. *Physical Review E*, 2004.
- Oran Lang, Yossi Gandelsman, Michal Yarom, Yoav Wald, Gal Elidan, Avinatan Hassidim, William T. Freeman, Phillip Isola, Amir Globerson, Michal Irani, and Inbar Mosseri. Explaining in Style: Training a GAN to explain a classifier in StyleSpace. In *International Conference on Computer Vision*, 2021.
- Hsin-Ying Lee, Hung-Yu Tseng, Jia-Bin Huang, Maneesh Kumar Singh, and Ming-Hsuan Yang. Diverse Image-to-Image Translation via Disentangled Representations. In *European Conference on Computer Vision*, 2018.
- Xiao Liu, Pedro Sanchez, Spyridon Thermos, Alison Q. O’Neil, and Sotirios A. Tsaftaris. Learning disentangled representations in the imaging domain. *Medical Image Analysis*, 2022.
- Francesco Locatello, Stefan Bauer, Mario Lucic, Gunnar Raetsch, Sylvain Gelly, Bernhard Schölkopf, and Olivier Bachem. Challenging Common Assumptions in the Unsupervised Learning of Disentangled Representations. In *Proceedings of the 36th International Conference on Machine Learning*, 2019.
- Christos Louizos, Kevin Swersky, Yujia Li, Max Welling, and Richard Zemel. The Variational Fair Autoencoder, 2017.
- Lars Mescheder, Sebastian Nowozin, and Andreas Geiger. Which Training Methods for GANs do actually Converge? In *International Conference on Machine Learning*, 2018.
- Mehdi Mirza and Simon Osindero. Conditional Generative Adversarial Nets, 2014.
- Takeru Miyato and Masanori Koyama. cGANs with Projection Discriminator. In *International Conference on Learning Representations*, 2018.
- Daniel Moyer, Shuyang Gao, Rob Brekelmans, Greg Ver Steeg, and Aram Galstyan. Invariant Representations without Adversarial Training. In *Advances in Neural Information Processing Systems*, 2018.
- Sarah Müller, Holger Heidrich, Lisa M. Koch, and Philipp Berens. fundus circle cropping, 2023. URL https://github.com/berenslab/fundus_circle_cropping.
- Weili Nie, Tero Karras, Animesh Garg, Shoubhik Debnath, Anjul Patney, Ankit B. Patel, and Anima Anandkumar. Semi-Supervised StyleGAN for Disentanglement Learning. In *Proceedings of the 37th International Conference on Machine Learning*, 2020.

- Simon Nusinovici, Tyler Hyungtaek Rim, Marco Yu, Geunyoung Lee, Yih-Chung Tham, Ning Cheung, Crystal Chun Yuen Chong, Zhi Da Soh, Sahil Thakur, Chan Joo Lee, et al. Retinal photograph-based deep learning predicts biological age, and stratifies morbidity and mortality risk. *Age and ageing*, 2022.
- Augustus Odena, Christopher Olah, and Jonathon Shlens. Conditional Image Synthesis With Auxiliary Classifier GANs. In *Proceedings of the 34th International Conference on Machine Learning*, 2017.
- Jiahong Ouyang, Ehsan Adeli, Kilian M. Pohl, Qingyu Zhao, and Greg Zaharchuk. Representation Disentanglement for Multi-modal brain MR Analysis. In *Information Processing in Medical Imaging*, 2021.
- Gaurav Parmar, Richard Zhang, and Jun-Yan Zhu. On Aliased Resizing and Surprising Subtleties in GAN evaluation. In *Conference on Computer Vision and Pattern Recognition*, 2022.
- Adam Paszke, Sam Gross, Francisco Massa, Adam Lerer, James Bradbury, Gregory Chanan, Trevor Killeen, Zeming Lin, Natalia Gimelshein, Luca Antiga, Alban Desmaison, Andreas Köpf, Edward Yang, Zach DeVito, Martin Raison, Alykhan Tejani, Sasank Chilamkurthy, Benoit Steiner, Lu Fang, Junjie Bai, and Soumith Chintala. PyTorch: An Imperative Style, High-Performance Deep Learning Library, 2019.
- Palvin G. Poličar, Martin Stražar, and Blaž Zupan. opentsne: a modular Python library for t-SNE dimensionality reduction and embedding. 2019.
- Ben Poole, Sherjil Ozair, Aaron Van Den Oord, Alex Alemi, and George Tucker. On Variational Bounds of Mutual Information. In *Proceedings of the 36th International Conference on Machine Learning*, 2019.
- Ryan Poplin, Avinash V Varadarajan, Katy Blumer, Yun Liu, Michael V McConnell, Greg S Corrado, Lily Peng, and Dale R Webster. Prediction of cardiovascular risk factors from retinal fundus photographs via deep learning. *Nature biomedical engineering*, 2018.
- Adalberto Claudio Quiros, Roderick Murray-Smith, and Ke Yuan. PathologyGAN: Learning deep representations of cancer tissue. In *Proceedings of the Third Conference on Medical Imaging with Deep Learning*, 2021.
- Anand E Rajesh, Abraham Olvera-Barrios, Alasdair N Warwick, Yue Wu, Kelsey V Stuart, Mahantesh Biradar, Chuin Ying Ung, Anthony P Khawaja, Robert Luben, Paul J Foster, Cecilia S Lee, Adnan Tufail, Aaron Y Lee, Catherine Egan, and EPIC Norfolk, UK Biobank Eye and Vision Consortium. Ethnicity is not biology: retinal pigment score to evaluate biological variability from ophthalmic imaging using machine learning, 2023.
- Tyler Hyungtaek Rim, Geunyoung Lee, Youngnam Kim, Yih-Chung Tham, Chan Joo Lee, Su Jung Baik, Young Ah Kim, Marco Yu, Mihir Deshmukh, Byoung Kwon Lee, et al. Prediction of systemic biomarkers from retinal photographs: development and validation of deep-learning algorithms. *The Lancet Digital Health*, 2020.
- Tyler Hyungtaek Rim, Chan Joo Lee, Yih-Chung Tham, Ning Cheung, Marco Yu, Geunyoung Lee, Youngnam Kim, Daniel SW Ting, Crystal Chun Yuen Chong, Yoon Seong Choi, et al. Deep-learning-based cardiovascular risk stratification using coronary artery calcium scores predicted from retinal photographs. *The Lancet Digital Health*, 2021.
- Karsten Roth, Mark Ibrahim, Zeynep Akata, Pascal Vincent, and Diane Bouchacourt. Disentanglement of Correlated Factors via Hausdorff Factorized Support. In *International Conference on Learning Representations*, 2023.
- Charumathi Sabanayagam, Dejiang Xu, Daniel SW Ting, Simon Nusinovici, Riswana Banu, Haslina Hamzah, Cynthia Lim, Yih-Chung Tham, Carol Y Cheung, E Shyong Tai, et al. A deep learning algorithm to detect chronic kidney disease from retinal photographs in community-based populations. *The Lancet Digital Health*, 2020.
- Dino Sejdinovic, Bharath Sriperumbudur, Arthur Gretton, and Kenji Fukumizu. Equivalence of distance-based and RKHS-based statistics in hypothesis testing. *The Annals of Statistics*, 2013.
- Karen Simonyan and Andrew Zisserman. Very Deep Convolutional Networks for Large-Scale Image Recognition. 2015.
- Jaemin Son, Joo Young Shin, Eun Ju Chun, Kyu-Hwan Jung, Kyu Hyung Park, and Sang Jun Park. Predicting high coronary artery calcium score from retinal fundus images with deep learning algorithms. *Translational Vision Science & Technology*, 2020.
- Taiji Suzuki, Masashi Sugiyama, Jun Sese, and Takafumi Kanamori. Approximating Mutual Information by Maximum Likelihood Density Ratio Estimation. In *Proceedings of the Workshop on New Challenges for Feature Selection in Data Mining and Knowledge Discovery at ECML/PKDD 2008*, 2008.

- Gábor J. Székely, Maria L. Rizzo, and Nail K. Bakirov. Measuring and testing dependence by correlation of distances. *The Annals of Statistics*, 2007.
- Frederik Träuble, Elliot Creager, Niki Kilbertus, Francesco Locatello, Andrea Dittadi, Anirudh Goyal, Bernhard Schölkopf, and Stefan Bauer. On Disentangled Representations Learned From Correlated Data. In *Proceedings of the 38th International Conference on Machine Learning*, 2021.
- Michael Tschannen, Olivier Bachem, and Mario Lucic. Recent Advances in Autoencoder-Based Representation Learning. In *Bayesian Deep Learning Workshop, NeurIPS*, 2018.
- Rachel Marjorie Wei Wen Tseng, Tyler Hyungtaek Rim, Eduard Shantsila, Joseph K Yi, Sungha Park, Sung Soo Kim, Chan Joo Lee, Sahil Thakur, Simon Nusinovici, Qingsheng Peng, et al. Validation of a deep-learning-based retinal biomarker (Reti-CVD) in the prediction of cardiovascular disease: data from UK Biobank. *BMC medicine*, 2023.
- T David Williams. Reflections from the Retinal Surface: Some Clinical Implications. *Canadian Journal of Optometry*, 1982.
- Wei Xiao, Xi Huang, Jing Hui Wang, Duo Ru Lin, Yi Zhu, Chuan Chen, Ya Han Yang, Jun Xiao, Lan Qin Zhao, Ji-Peng Olivia Li, et al. Screening and identifying hepatobiliary diseases through deep learning using ocular images: a prospective, multicentre study. *The Lancet Digital Health*, 2021.
- Qizhe Xie, Zihang Dai, Yulun Du, Eduard Hovy, and Graham Neubig. Controllable Invariance through Adversarial Feature Learning. In *Advances in Neural Information Processing Systems*, 2017.

6 Appendix

6.1 Toy example for disentanglement loss

Although distance correlation is simple to compute, it is able to measure nonlinear dependencies between variables. With a simple toy example we show how distance correlation handles dependencies between subspaces compared to two linear dependency measures. We sampled 1,000 points from two 2-dimensional subspaces $w_1 = [w_{1,1}, w_{1,2}] \in \mathbb{R}^2$ and $w_2 = [w_{2,1}, w_{2,2}] \in \mathbb{R}^2$ and created dependencies between them (Fig. 14 a, main diagonals in the pair plots). We defined an optimization problem, where points should be moved in order to minimize different dependence measures (Fig. 14 b-d). We optimized point coordinates with PyTorch (Paszke et al., 2019) and an Adam optimizer ($\beta_1 = 0.9, \beta_2 = 0.99, \epsilon = 10^{-8}$) with a learning rate of 0.05 for 500 steps. When we optimize for linear dependence measures like Gaussian mutual information (GMI) or collapsed Gaussian mutual information (C-GMI) the dependence measure only decreased for linear dependencies (Fig. 14 b,c, distance correlation values below points). GMI and C-GMI are two mutual information estimators that assume that the subspace vectors w_1 and w_2 follow a multivariate normal distribution. For a detailed background on GMI and C-GMI, see the next Sec. 6.2. However, when we optimized for distance correlation, the dependence measure also dropped for nonlinear dependencies (Fig. 14 d, distance correlation values below points).

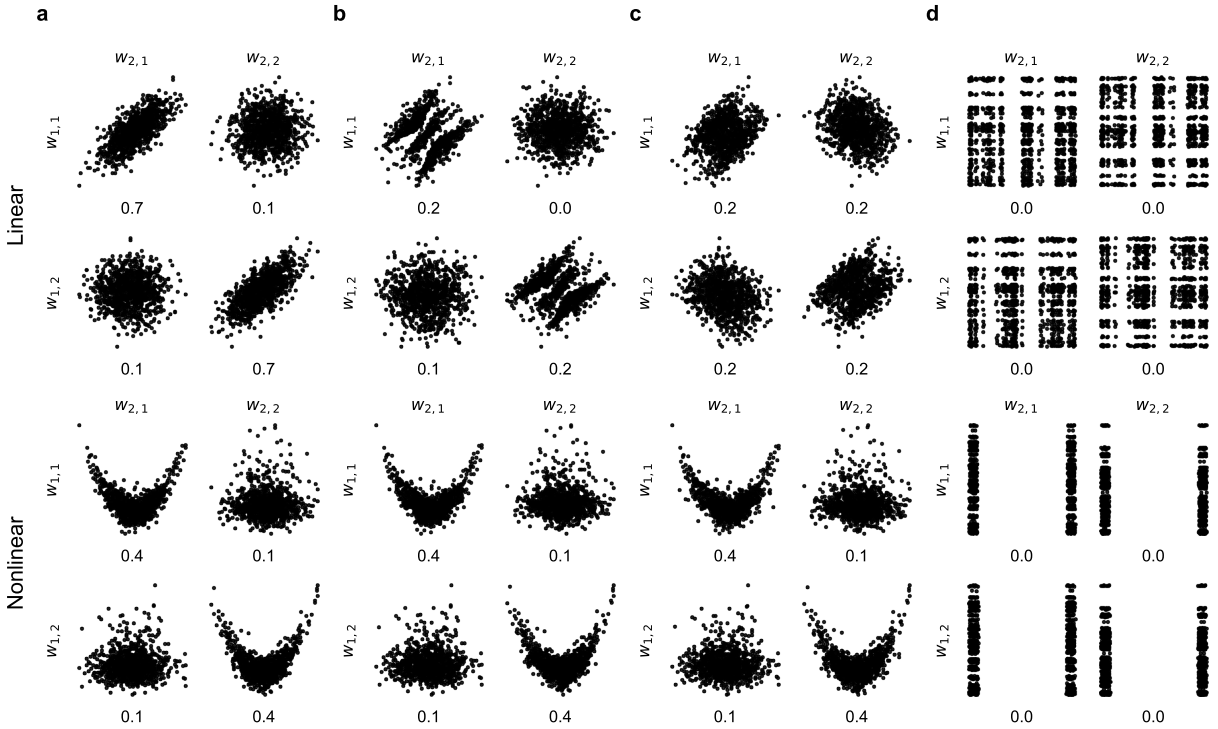


Figure 14: Toy example for different dependency measures. We sampled 1,000 points from two 2-dimensional subspaces $w_1 = [w_{1,1}, w_{1,2}] \in \mathbb{R}^2$ and $w_2 = [w_{2,1}, w_{2,2}] \in \mathbb{R}^2$ and created dependencies between the main diagonals in the pair plots of **a**. We defined an optimization problem where we changed point coordinates to minimize various dependency measures. Below the points we show distance correlation as a dependence measure. In panels **b** and **c** we show the displacement of points when minimizing the linear dependency measures GMI and C-GMI, respectively. In panel **d** we see that, compared to GMI and C-GMI, distance correlation can also effectively disentangle nonlinear dependencies between subspaces.

6.2 Gaussian mutual information

Mutual information (MI) between two random vectors is defined as

$$\text{MI}(w_1, w_2) = D_{\text{KL}}(p(w_1, w_2) || p(w_1)p(w_2)).$$

When we assume the subspace vectors follow a multi-variate normal distribution $w_1 \sim \mathcal{N}(\mu_1, \Sigma_1)$ and $w_2 \sim \mathcal{N}(\mu_2, \Sigma_2)$, the MI simplifies to

$$\begin{aligned} \text{GMI}(w_1, w_2) &= D_{\text{KL}}(p(w_1, w_2) || p(w_1)p(w_2)) \\ \text{GMI}(w_1, w_2) &= \frac{1}{2} \left(\log \left(\frac{\det \Sigma_1 \det \Sigma_2}{\det \Sigma} \right) \right) \end{aligned}$$

which we call a Gaussian mutual information (GMI). Here, Σ is the covariance matrix of the joint distribution $p(w_1, w_2)$

$$\Sigma = \begin{pmatrix} \Sigma_{w_1} & \Sigma_{w_1, w_2} \\ \Sigma_{w_1, w_2} & \Sigma_{w_2} \end{pmatrix}$$

Approximating this measure over batches leads to numerical instabilities for covariance matrix estimation. Hence, we simplify the computation even more by taking the sum of the variables over their feature dimension $\hat{w}_1 = \sum_{i=0}^{d_1} w_{1,i}$ and $\hat{w}_2 = \sum_{i=0}^{d_2} w_{2,i}$. Since we collapse feature dimensions here, we name this measure collapsed Gaussian mutual information (C-GMI).

$$\text{C-GMI}(w_1, w_2) = \frac{1}{2} \log \left(\frac{\text{var}(\hat{w}_1) \text{var}(\hat{w}_2)}{\text{var}(\hat{w}_1) \text{var}(\hat{w}_2) - \text{cov}(\hat{w}_1, \hat{w}_2)^2} \right)$$

Linear dependency measure. When we assume w_1 and w_2 follow a multi-variate normal distribution, the measure GMI measure is only dependent on the covariance Σ of the joint distribution $p(w_1, w_2)$

$$\text{GMI}(w_1, w_2) = \text{GMI}(\Sigma) = \frac{1}{2} \left(\log \left(\frac{\det \Sigma_{w_1} \det \Sigma_{w_2}}{\det \Sigma} \right) \right)$$

Hence, this measure considers only linear dependencies in the uncollapsed and collapsed form.

6.3 Experimental details for encoder training

We trained a Resnet-18 encoder (He et al., 2016) from scratch, where we added to the output feature map a ReLU and a linear layer mapping to the latent representation $win\mathcal{W}$. We set $\lambda_{DC} = 0.5$, a batch size of 512 using the Adam optimizer ($\beta_1 = 0.9, \beta_2 = 0.99, \epsilon = 10^{-8}$) with a learning rate of 1e-3 for 100 epochs. To avoid overfitting, we used a weight decay of 8e-3. We trained on two 2080 Ti GPUs for 5-6 hours with the PyTorch Lightning framework (Falcon and The PyTorch Lightning team, 2019). We chose the best model in terms of total validation loss (early stopping) for evaluation. For t-SNE visualization we used openTSNE (Poličar et al., 2019) with an euclidean metric and a perplexity of $n_p/100$, where n_p is the number of data points.

6.4 Experimental details for generative model training

In practice, we trained our GAN models on multiple GPUs. The standard setup in PyTorch Lightning (Falcon and The PyTorch Lightning team, 2019) for multi GPU training is the Distributed Data Parallel (DDP) strategy. In DDP, each GPU trains with its own data and synchronize the gradients with all other GPUs. Therefore, each GPU only processes a subset of the whole data batch. However, the batch size is an integral part of the distance correlation estimation (Sec. 3.3). Therefore, we introduced a data ring buffer on every GPU that stores a number of data batches from the past for distance correlation computation.

We train our model with StyleGAN’s style mixing (Karras et al., 2020), which is a regularization technique for disentanglement where images are generated from two different latent vectors that are fed to the generator at different resolution levels. It becomes impractical to train the GAN-inversion in these steps because images generated with style mixing (Quiros et al., 2021). Therefore, we optimize for GAN-inversion only when the generator is not trained with style mixing regularization (Karras et al., 2020). We ended up performing style-mixing regularization only 50% of the time instead of 90% as in the original StyleGAN2 implementation. Thus, on average, the GAN-inversion losses are included in every second optimization step.

For the generative image model we set $\lambda_{PL} = 2$, $\lambda_w = 1$, $\lambda_p = 2$, $\lambda_C = 0.04$ and $\lambda_{DC} = 0.04$. To set λ_{R_1} we used a heuristic formula from the original StyleGAN2 implementation which is $\lambda_{R_1} = 0.0002 \cdot 256 / (n \cdot g)$ where 256 is the image size, n is the batch size and g is the number of GPUs. The mapping networks had 8 fully connected layers. We trained with a batch size of 56 distributed over 4 GPUs, where on each GPU we had a data ring buffer storing 5 batches (4 batches from the past) for distance correlation computation. For the generator and the discriminator we used individual Adam optimizers, each with a learning rate of 2.5e-3 and hyperparameters $\beta_1 = 0.9, \beta_2 = 0.99, \epsilon = 10^{-8}$. We trained each generative model for 200 epochs on four V100 GPUs for 2.5 days with the PyTorch Lightning framework (Falcon and The PyTorch Lightning team, 2019). For evaluation, we chose the best model in terms of total validation loss (early stopping). For t-SNE visualization we used openTSNE (Poličar et al., 2019) with an euclidean metric and a perplexity of $n_p/100$, where n_p is the number of data points.

6.5 Experimental details on controllable image generation

For the age classification model, we trained a Resnet-18 encoder (He et al., 2016) from scratch, where we added to the output feature map a ReLU and a linear layer mapping to the predicted logits $\hat{y} \in \mathbb{R}^3$. We trained the

classification model for the 3-class age problem on the reconstructions, since we may have a distribution shift between the real images and the reconstructions. For testing, we swapped age subspaces by first shuffling the test dataset in a deterministic manner and then swapping the age subspaces with a shift of one in each batch. Therefore, each batch element was assigned the age subspace of its predecessor, while the first batch element was assigned the age subspace of the last batch element.